

High-resolution structures of the M2 channel from influenza A virus reveal dynamic pathways for proton stabilization and transduction

Jessica L. Thomaston^a, Mercedes Alfonso-Prieto^b, Rahel A. Woldeyes^a, James S. Fraser^c, Michael L. Klein^b, Giacomo Fiorin^{b,1}, and William F. DeGrado^{a,1}

^aDepartment of Pharmaceutical Chemistry, University of San Francisco, San Francisco, CA 94158; ^bInstitute of Computational Molecular Science, Temple University, Philadelphia, PA 19122; and ^cDepartment of Bioengineering and Therapeutic Science, University of California, San Francisco, San Francisco, CA 94158

Contributed by William F. DeGrado, October 7, 2015 (sent for review April 21, 2015; reviewed by Vadim Cherezov and Douglas J. Tobias)

The matrix 2 (M2) protein from influenza A virus is a proton channel that uses His37 as a selectivity filter. Here we report high-resolution (1.10 Å) cryogenic crystallographic structures of the transmembrane domain of M2 at low and high pH. These structures reveal that waters within the pore form hydrogen-bonded networks or “water wires” spanning 17 Å from the channel entrance to His37. Pore-lining carbonyl groups are well situated to stabilize hydronium via second-shell interactions involving bridging water molecules. In addition, room temperature crystallographic structures indicate that water becomes increasingly fluid with increasing temperature and decreasing pH, despite the higher electrostatic field. Complementary molecular dynamics simulations reveal a collective switch of hydrogen bond orientations that can contribute to the directionality of proton flux as His37 is dynamically protonated and deprotonated in the conduction cycle.

proton channels | influenza M2 channel | membrane proteins

Proton transport and conduction is essential to life. Proteins conduct protons over long distances through membranes to facilitate proton-coupled electron transfer and the formation and utilization of proton gradients. The M2 proton channel from the influenza A virus (1) is not only a medically important protein but also a simple, well-defined system for studying proton transport through confined spaces (2–4). This channel is the target of the anti-flu drug amantadine. M2 is activated at low pH by protonation of His37, which also participates in proton conduction by shuttling protons into the interior of the virus (5–7). His37 lies near the center of the bilayer, where it is connected to the viral exterior by a water-filled pore through which protons must pass to gain access to the viral interior (8–13).

Visualizing the flow of protons within protein channels such as M2 is one of the long-standing challenges in molecular biophysics. Based on computational studies (9, 14–19) it has been suggested that protons reach His37 through “water wires” via the Grotthuss mechanism, but there is little high-resolution information concerning the path by which protons are conducted. A previously solved 1.65-Å crystal structure (9) showed six ordered waters immediately above the His37 tetrad, but ordered waters spanning the entire aqueous pore of M2 have not been observed until now. Previous MD simulations suggested a pore with mobile waters (12, 15), whereas the results of NMR and IR experiments are more consistent with an environment that is more similar to bulk water at low pH (13, 19, 20). However, it is difficult to deconvolute the changes in the water structure and dynamics when the protonation of His37 is raised from those induced indirectly via the conformation of the protein’s main chain.

The M2 channel is known to have at least two conformational states that are populated to differing extents at low versus high pH (1, 10, 12). One, seen primarily at high pH, has been characterized extensively by solution NMR (21, 22), solid-state NMR (SSNMR) (10, 12), and X-ray crystallography (9). A second form

is observed in dynamic equilibrium at lower pH (21–23), as evidenced by a broadening of magnetic resonances that thus far has made it impractical to determine a high-resolution structure of the protein in this state by SSNMR or solution NMR. X-ray crystallographic studies, however, have provided structures of both states (8, 9), which differ primarily in the conformation of the C terminus where protons exit the channel. Here we have obtained crystals that diffract to high resolution (1.10 Å) at both low and high pH, allowing visualization of water wires leading to His37 as a function of pH. The conformations of the backbone at the two pH values are essentially identical, permitting us to isolate changes in the organization of the water without any confounding factors.

Results and Discussion

High-Resolution Structures of M2TM. In this work, we use a minimal construct, M2TM, which is fully active as a proton channel (24). M2TM was crystallized using lipidic cubic phase (LCP) techniques, which provide a continuous lipid bilayer in which crystallization can occur (25). Indeed, the channel is surrounded by a layer of monoolein molecules, and very few protein–protein interactions are present in the crystal lattice (*SI Appendix*, Fig. S1).

Significance

The conduction of protons through the highly restricted paths of transmembrane proteins is an essential process of living systems and an intriguing problem in modern physical chemistry. The small size of the influenza M2 proton channel makes it an ideal system for the study of proton transport across a membrane. Additionally, the M2 channel has medical relevance as an anti-flu drug target. These high-resolution structures of the channel were obtained by crystallizing the protein in a membrane-like environment and reveal networks of hydrogen-bonded waters that change with temperature and pH. The locations of these waters, in conjunction with molecular dynamics simulations that predict their hydrogen bond orientations, provide insight into the mechanism of proton stabilization and transduction within the channel.

Author contributions: J.L.T., M.A.-P., J.S.F., M.L.K., G.F., and W.F.D. designed research; J.L.T. and M.A.-P. performed research; J.L.T., M.A.-P., R.A.W., J.S.F., M.L.K., G.F., and W.F.D. analyzed data; and J.L.T., M.A.-P., R.A.W., J.S.F., M.L.K., G.F., and W.F.D. wrote the paper.

Reviewers: V.C., University of Southern California; and D.J.T., University of California, Irvine.

The authors declare no conflict of interest.

Data deposition: The atomic coordinates have been deposited in the Protein Data Bank, www.pdb.org (PDB ID codes 4QK7, 4QKC, 4QKM, and 4QKL).

¹To whom correspondence may be addressed. Email: william.degrado@ucsf.edu or giacomo.fiorin@temple.edu.

This article contains supporting information online at www.pnas.org/lookup/suppl/doi:10.1073/pnas.1518493112/-DCSupplemental.

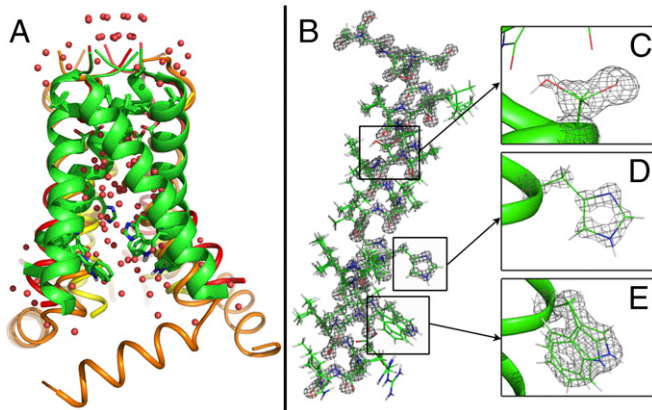


Fig. 1. Crystal structure of M2TM at 1.10 Å at pH 8.0 (4QK7) under cryogenic conditions. (A) Superposition of this structure (green) with previously solved structures of M2 2LOJ (12) (orange), 3LBW (9) (yellow), and 3BKD (8) (red) shows that the conformation of the N-terminal half of the channel is relatively conserved whereas the conformation of the C terminus varies. Waters from the high-pH cryogenic structure (red spheres) are overlaid with waters from the low-pH cryogenic structure (pink spheres). (B) Density of backbone and side chains of a monomer of M2TM at a contour of 3.0 σ shows features typical of high-resolution structures. (C) Ser31 side chain (conformer A and B) at a contour of 1.0 σ. (D) His37 side chain at a contour of 3.0 σ. (E) Trp41 side chain (conformer A and B) at a contour of 1.5 σ.

The conformation of the protein (Fig. 1A) lies between the C-terminally closed conformation previously seen in several crystal and NMR structures (9, 10, 12, 21, 22) and a conformation with a dilation of the C-terminal end of the pore seen in some crystal structures (8). The primary focus of the current study is on the water-filled pore leading to His37, whose backbone structure is very similar in all previously solved structures of M2, including a structure of a longer construct determined by SSNMR in phospholipid bilayers (12) (Fig. 1A). However, the current structures include a complete set of water molecules in the pore and were resolved at exceptional resolution (1.1 Å); fewer than 10 structures of membrane proteins have been defined to less than a 1.2-Å resolution, and the present structures are also, to our knowledge, among the first high-resolution structures of a membrane protein near room temperature. Because of their high resolution, these structures provide novel insights into the water molecules that work in concert with the protein macromolecule to affect biological proton transport.

Crystals were grown at pH 8.0 (“high pH”) and 5.5 (“low pH”) and crystallographic data were collected at cryogenic and room temperatures (*SI Appendix*, Table S1). Although the conformations of the backbone and even most side chains are essentially identical between the structures, there are marked differences in the distribution and occupancy of solvent molecules as a function of pH and temperature throughout the channel in the N-terminal pore leading to His37. The cryo-cooled structures were solved to a 1.10-Å resolution and show electron density maps typical of high-resolution structures, including features from the hydrogen atoms of CH bonds (Fig. 1 B–E). As in a previous crystallographic structure (9) and consistent with SSNMR (10, 11), water molecules bind to both the delta and epsilon nitrogens of His37. The N-terminal part of the pore is occluded by four Val27 residues, but it is possible for protons entering from the outside of the virus to gain access to water in the pore via low-energy fluctuations of the Val27 residues (19, 26).

A Multitude of Water Wires Lead to His37. The cryo structures determined at high pH (4QK7) and low pH (4QKC) show multiple continuous paths of water molecules stretching ~17 Å from Val27 to His37 (Fig. 2). Some water molecules are found at full

occupancy, whereas others are found at one of two closely adjoining sites that together add up to full occupancy. The water wires have multiple branching points that create multiple hydrogen bond pathways by which a proton can pass through the pore en route to one of the four His37 residues. Thus, the low-temperature structures (~100 K) identify a highly degenerate path of enthalpically stable (27) water wires.

Fluid Water Wires at Room Temperature. To determine whether additional paths would be present near room temperature, two additional structures were determined at 273 K at high pH (4QKL) and low pH (4QKM) to 1.71- and 1.44-Å resolution, respectively. The electron density maps for the room temperature conditions versus the cryo temperature conditions, calculated to a common resolution, show a number of striking similarities and also differences in electron density originating from water in the pore (Fig. 3 A and B; *SI Appendix*, Fig. S2). Water molecules remain bound to the highly conserved His37 residue, but higher variability is seen across the other pore-lining water molecules. At pH 8, a clathrate-like structure is observed below Val27 and is anchored by hydrogen bonds to the main chain carbonyls facing the pore, but the water layer connecting to the hydrated His37 residues has become too diffuse to be seen clearly in the electron density. At pH 5.5, the water density in most of the pore is diffuse and a fully connected hydrogen bond network can not be observed. The water in this region is disordered, indicating that the wires seen at low temperature represent snapshots of the energetically most favorable pathways among a larger ensemble of dynamically exchanging sites populated at room temperature.

An Abundance of Hydrogen-Bond Donors Relative to Acceptors in the Channel. The pore of the protein is richer overall in hydrogen bond acceptors than in donors. This presents an environment that should intrinsically stabilize a hydronium ion, which has three hydrogen bond donors and only one relatively weak acceptor. The water molecules in the channel form hydrogen bonds with the accepting carbonyl groups of Gly34, Ala30, and Val27. The hydroxyl group of Ser31 donates an intramolecular hydrogen bond to a carbonyl in the helix, leaving its two electron lone pairs free to accept hydrogen bonds from water molecules in the pore. At high pH, the δ-nitrogen of His37 also presents a hydrogen bond acceptor (7, 11), although this residue switches to being a donor with protonation at low pH. Thus, the channel would appear to be intrinsically suited to stabilize hydronium in the pore, particularly when His37 residues are in the neutral state. This environment is consistent with the idea that M2-blocking drugs, such as amantadine and rimantadine, act as substrate analogs of the hydronium ion due to their positively charged ammonium groups and lack of hydrogen bond acceptors (28).

Density of Water by Molecular Dynamics Simulations. To gain further insight into the water network inside the M2 pore and its response to pH changes (i.e., the protonation state of His37), we performed force field-based molecular dynamics (MD) simulations of the hydrated protein crystals (*SI Appendix*, Figs. S3–S5) at a temperature of 310 K as in other simulations of M2TM (9). Computational studies of different proteins have shown that MD simulations in a crystal environment yield water densities in good agreement with experimentally determined electron densities (29–32). Additionally, MD simulations can complement the X-ray data by providing an atomic picture of the water hydrogens and their H-bonding connectivity and dynamics, as recently shown for aquaporin (4). The highest calculated density of water is near His37 and the pore-facing carbonyls of residue 34 (Fig. 3), similarly to what is indicated by the present structures and by the previous X-ray structure of M2TM (9). In addition to these, simulations also predict the presence of water molecules at other positions (*SI Appendix*, Fig. S2), including molecules that are not

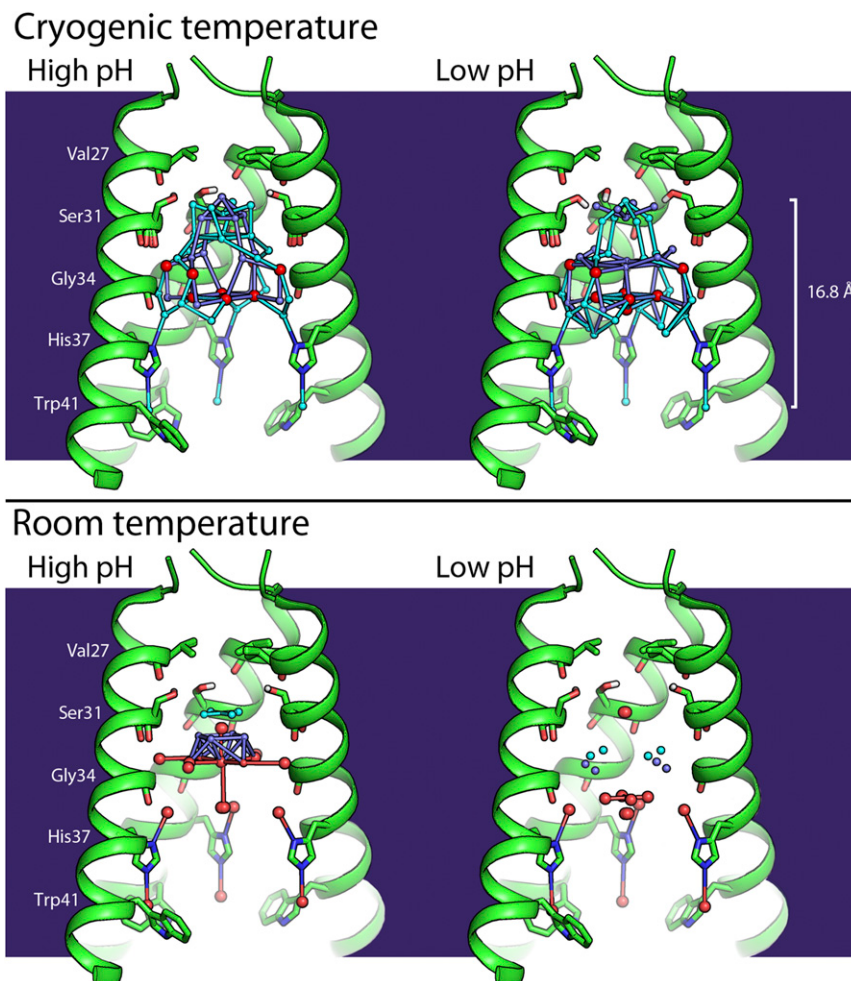


Fig. 2. Waters in the cryogenic crystal structures form ordered water wires whereas room temperature waters are less ordered. The front helix of each tetramer has been removed. (*Top*) Water wires inferred from crystallographic water positions from the 1.10-Å resolution cryo crystal structures at pH 8.0 (*Left*, PDB code 4QK7) and pH 5.5 (*Right*, PDB code 4QKC) form a continuous network of water wires within the N-terminal half of the pore leading to the gating His37 residue, with some positional changes in the waters between the two pH conditions. Alternate occupancy water-wire networks A (light blue) and B (dark blue) intersect at full occupancy waters (red). Continuous water wires span 16.8 Å of the channel pore. (*Bottom*) Water networks observed under room temperature conditions at pH 8.0 at a 1.71-Å resolution (*Left*, PDB code 4QKL) and pH 5.5 at a 1.44-Å resolution (*Right*, PDB code 4QKM) have fewer ordered waters and no longer form a continuous path leading to His37; in the low-pH structure, the waters do not form ordered networks at all and instead appear fluid-like.

in direct contact with the protein's side chains. Although the measured and calculated densities bear many similarities, it is possible that the mismatches between the two may affect the calculation of the hydrogen positions. To assess this potential issue, we also performed control simulations with all water molecules restrained at their crystallographic positions: these yield nearly identical distributions of donors and acceptors of H-bonds as when water molecules are left free to diffuse in the pore (*SI Appendix*, Fig. S10).

Hydrogen Bond Network Within the M2 Pore. The M2 proton channel has the interesting property of being an asymmetric conductor: it conducts protons from the outside to the inside of the virus when the outside pH is low (as in an acidifying endosome), but does not as easily conduct protons outward when the pH gradient is reversed. The current crystallographic structures and MD simulations provide a detailed molecular description for this behavior. As the protonation state of the His37 changes, the polarity of the H-bonds between water molecules becomes increasingly aligned with the axis of the channel (*SI Appendix*, Fig. S6 and Table S2). The total number of H-bonds is higher in

the charge states of the histidine tetrad accessible at high pH (0 and 1⁺) than in the higher charge states populated at low pH (3⁺ and 4⁺). Nevertheless, the H-bonds in the high pH states do not adopt a preferred orientation, whereas in the low-pH states all H-bonds are highly directional. In the 3⁺ and 4⁺ charge states (Fig. 4C and *SI Appendix*, Fig. S7H), the H-bonds are oriented outward in the extraviral half of the pore and are oriented inward in the intraviral half. The change of polarity occurs at His37 (*SI Appendix*, Fig. S8). The protonated His can donate two H-bonds, one upward to the water molecules in the extraviral side of the pore and one downward to the water molecules in the intraviral side. In contrast, in the 0 and 1⁺ states (Fig. 4B and *SI Appendix*, Fig. S7E), the water molecules can form both outward- and inward-oriented H-bonds with their neighbors regardless of their position along the pore, and the flipping between the two orientations occurs in the subnanosecond timescale. Except for the immediate vicinity of His37, the high-pH pore exhibits only mild imbalances between outward- and inward-oriented H-bonds (*SI Appendix*, Fig. S6). In other words, the H-bond network inside the M2 pore can be described as an assembly of “loopback circuits” at high pH and as a single

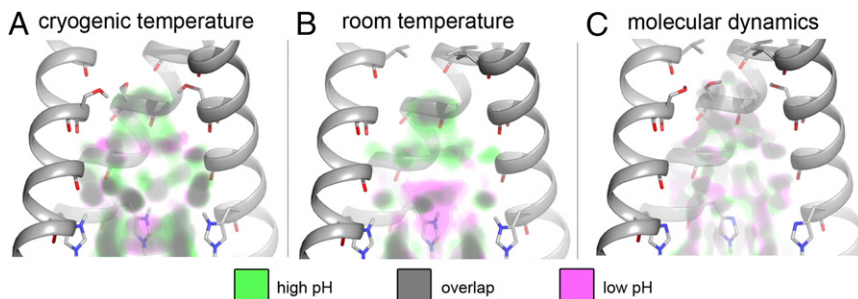


Fig. 3. Electron density comparisons show differences and similarities between the solvent density at high and low pH. The front helices have been removed. Electron density at a contour of 1.5 sigma under (A) cryogenic conditions, (B) room temperature conditions, and (C) calculated electron density from molecular dynamics simulations is shown for both high (green) and low (magenta) pH experiments/simulations (high pH corresponds to a neutral His37 cluster, and low pH to a 4⁺ charge state). Areas where low- and high-pH densities overlap are shown in gray. Electron density from water binding to carbonyl groups and histidines is relatively conserved under all conditions whereas variations in density are seen elsewhere.

“parallel circuit” at low pH. The switch between the two configurations takes place at the 2⁺ charge state (*SI Appendix*, Fig. S7 F and G), which is most populated at neutral pH (7, 24).

We compared this behavior with analogous simulations of the two most prevalent M2 mutants, S31N-M2TM and D44N-M2TM (33), in the same unit cell [S31N-M2TM crystallizes in the LCP with unit-cell parameters within 1 Å from those shown here (22), and the backbone of D44N-M2TM modeled by MD and NMR (34) is at less than 2 Å rmsd from the current structures]. S31N-M2TM also exhibits “loopback circuits” at high pH (*SI Appendix*, Figs. S13–S15), but D44N-M2TM features a “parallel circuit” configuration at all pH levels (*SI Appendix*, Figs. S19–S21). Electrophysiology experiments showed that WT-M2 and S31N-M2 have similar pH/current profiles (33), but the proton conductance of D44N-M2 saturates below pH 5 (34). Thus, the “loopback circuits” appear to correlate with the ability to promote the addition of protons onto a charged His37 cluster. A similar H-bond network structure was also seen for the water molecules adjacent to His37 in the previous 1.65-Å crystal structure of M2TM (9).

Hydrogen-Bond Donor/Acceptor Water Molecules Along the M2 Pore.

As posited above, the M2 pore-lining residues are expected to act preferentially as H-bond acceptors, thus providing the ideal environment to stabilize a hydronium ion. Our MD simulations show that, in response, the water molecules behave preferentially as H-bond donors along the 17-Å stretch between Val27 and His37 (*SI Appendix*, Fig. S9). There is a larger net number of water molecules acting as H-bond donors on the extraviral side of the M2 pore, irrespective of the charge state of the histidine tetrad. In contrast, the H-bonding population in the C-terminal part of the pore (between Trp41 and Leu46) is highly sensitive to pH. In the neutral state, there is only a marginal preference for the water molecules to act as donors in the direction of proton influx. As the charge on the His37 tetrad increases, the water molecules switch into H-bond acceptors so that they can establish H-bonds with the protonated His37, which can donate two H-bonds (Fig. 4 and *SI Appendix*, Table S2). These interactions are also seen in the S31N- and D44N-M2TM simulations (*SI Appendix*, Tables S3 and S4 and Figs. S16 and S22), indicating that no significant changes in the H-bonds between protein and water are brought about by naturally occurring mutations.

Conclusions. It is interesting to compare the present studies of the M2 channel with previous studies of the water channel (4) and ammonia channel (3), both structures that have been solved at moderate to high resolution and are responsible for diffusion of solvent molecules. In the case of the ammonia and water channels, the conduction pore allows for diffusion of single molecules of

neutral H₂O or NH₃ while excluding ammonium or hydronium ions. In contrast, the selectivity filter of the M2 channel is formed by a general acid/base, His37, which shuttles protons through the channel. The conduction path leading to this selectivity filter in M2 is markedly different from the ammonia and water channels in that it is broader and able to conduct protons through partially occupied water wires. Although there are only ~16 water molecules at a given time in the path leading to His37, they are at partial occupancy at low temperature, giving rise to hundreds of potential paths conducive to proton conduction. The apparent fluid nature of the pore becomes even more apparent near room temperature, where the density suggests greater disorder, particularly at low pH. Moreover, examination of the structures and the predominant protonation state of His37 suggests that the overall collection of individual water molecules, although likely mobile, are on average highly polarized to favor hydrogen bond orientations that encourage entry of protons when the His37 residues are deprotonated; similarly, as His37 becomes more protonated,

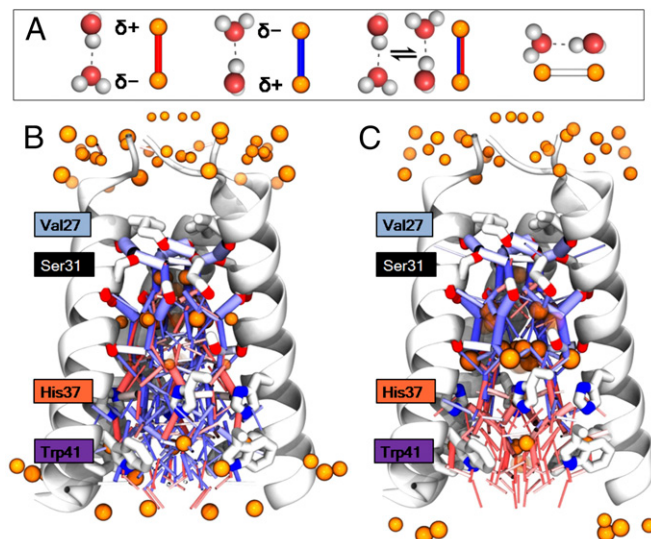


Fig. 4. Hydrogen bond orientation calculated from MD simulations. (A) Schematic representation of the water wires and the hydrogen bond orientation. The oxygens of water molecules observed in the room temperature X-ray structures are shown as van der Waals spheres (orange color) with diameter proportional to the crystallographic B-factors and transparency reflecting the partial occupancy. Hydrogen bonds are displayed as sticks with a color scale denoting their orientation and the thickness proportional to their population. (B) Water wires for a neutral channel. (C) Water wires at the 4⁺ charge state.

diffusion of protons into the channel might be encouraged. This dipolar switching might work in concert with rotameric switching to create the asymmetric proton conductance of the channel. Finally, the water molecules in the channel are surrounded by hydrogen bond-donating carbonyl groups, which should serve to stabilize hydronium through second-shell effects via bridging water molecules. It is encouraging that the present MD simulations in a crystal environment are consistent with experimental observations and add quantitative detail to these qualitative conclusions. Moreover, given the small size and biological relevance of the M2 channel, these structures should be ideally suited for more detailed simulations based on valence bond (15, 35) quantum and quantum mechanics/molecular mechanics simulations (14, 36) in which the formation and cleavage of covalent bonds associated with proton transfer can be examined in atomic detail.

Materials and Methods

Experimental Methods. The peptide construct used in this study is M2(22–46) from influenza A/Udorn/307/1972. The sequence, the molecular weight of which is 2682.268 Da (average), is as follows: Ac-SSDPLVVAASIIIGILHILWILDRL-NH₃. The peptide was synthesized manually at high temperature using Fmoc chemistry, cleaved from the resin and then purified using reverse-phase HPLC. The molecular weight of the desired product was confirmed using mass spectrometry, and the purity of the product was tested using analytical HPLC. The purified peptide was dissolved in ethanol and stored at –80 °C. The lipidic cubic phase was prepared with some modifications to the protocol described by Caffrey and Cherezov (38), and then crystallization conditions were screened in 96-well plastic sandwich plates. Square-shaped crystals belonging to space group I₄ formed after 2–4 wk of incubation at 10 °C. These conditions were optimized to grow 20- to 120-μm crystals. The crystals used for data collection at cryogenic conditions were grown in 96-well plates at 10 °C and then harvested into liquid nitrogen. The crystals used for room temperature data were grown in 96-well plates at 20 °C and then were transported to the beam line at ambient temperature for harvesting and data collection.

All crystallographic data were collected at the Advanced Light Source on beam 8.3.1. The beam size was 100 μm for all data sets; the detector used was a 3 × 3 CCD array (ADSC Q315r). Data from the two cryo condition crystals that diffracted to 1.1 Å were collected at a temperature of <100 K with a 13.0 keV beam and a detector-to-sample distance of 125 mm. The high-pH cryo condition crystal (PDB entry 4QK7) was exposed to the beam for 6 s per frame, and the low-pH cryo condition crystal (PDB entry 4QKC) was exposed for 4 s per frame; both crystals were oscillated 1° during data collection. The room temperature data were collected at 273 K using room temperature data collection techniques (38) with a 11.111-keV beam and an aluminum foil attenuator for both data sets. The crystals accumulated radiation damage faster under room temperature diffraction conditions, so larger crystals (50–120 μm) had to be used to obtain complete data sets. The low-pH room temperature condition crystal (PDB entry 4QKM) was exposed to the beam for 3 s per frame with a detector-to-sample distance of 125 mm; the high-pH room temperature condition crystal (PDB entry 4QKL) was exposed to the beam for 1 s per frame with a detector-to-sample distance of 150 mm; both crystals were oscillated 1° during data collection.

Data processing was done in iMosflm (39). Phasing was done by molecular replacement in the Phenix suite using Phaser MR (40) with chain A from PDB entry 3C9J (8) as a search model, and then refinement was carried out in Phenix Refine (17). Protein model manipulation and addition of water and ions were done in Coot (20), and monoolein molecules were manually fit

into Fo-Fc density using both Coot and PyMol (41). Alternate conformers were predicted using the qFit web server (25) and Ringer (42) and were also manually added where positive Fo-Fc density indicated that they were present. See *SI Appendix, Table S1*, for data processing and refinement statistics. Anisotropic B-factors were used for both cryo conditions (PDB entries 4QK7 and 4QKC) and the low-pH room temperature condition (PDB entry 4QKM) but not the high-pH room temperature condition (PDB entry 4QKL).

Molecular Dynamics Simulations. Classical MD simulations of the hydrated protein crystal were performed to study the network of water molecules inside the M2 pore and its response to pH changes (i.e., the protonation state of His37). The initial configurations were built using the two cryo X-ray structures of the transmembrane region of the M2 bundle solved either at low pH (PDB entry 4QKC) or high pH (PDB entry 4QK7). To model the I₄ symmetry of the crystal, two staggered tetramers were included in the simulation box (*SI Appendix, Fig. S3*), along with the crystallographically resolved water molecules. Simulations were performed starting from either of the solved structures for each of the five possible protonation states of the His37 tetrad (0, +1, +2, +3, and +4). The neutral histidine residues were set in the ε-tautomeric state, and the histidine charge was increased by protonating one, two (nonadjacent), three, or all four histidines, respectively, for each of the two tetramers. Each of the 10 resulting systems consists of ~7,000 atoms. The simulations were performed in the NVT ensemble at 310 K using the measured crystal lattice dimensions (29.310 × 29.310 × 67.310 Å for the low-pH structure and 29.536 × 29.536 × 66.853 Å for the high pH); periodic boundary conditions were applied to mimic the crystal environment. The protein was modeled using the CHARMM force field (29, 30) with correlation maps (CMAP) corrections (32), and the water molecules were described using the TIP3P model (43). All MD simulations were carried out with the NAMD program (44), and a production trajectory of ~350 ns was sampled for each system.

Analysis of the MD trajectories was performed over the last ~250 ns of the MD trajectories and enforcing fourfold rotational symmetry. Water densities (Fig. 3A) were obtained from the MD simulations using the Volmap plugin (45) in the VMD program (46). Populations of hydrogen-bonded water molecules (Fig. 4 and *SI Appendix, Fig. S7*) were calculated using the following clustering protocol. A hydrogen-bond vector was defined between a donor and an acceptor when the two oxygen atoms were at a distance less than 3.5 Å and the donor-hydrogen-acceptor angle was between 150° and 180°. The clusters of these vectors were calculated using g_cluster (47) with a 1.5-Å cutoff. The occupancy of a hydrogen bond represented by the centroid of one cluster was obtained by dividing the population of the cluster by the total number of MD frames and by 4 (to normalize upon symmetrization), such that the occupancy of a given hydrogen bond was at most 1. A similar protocol was used in Gianti et al. (48).

ACKNOWLEDGMENTS. Experimental work was funded by NIH Grant R01-GM056423. Use of the lipidic cubic phase crystallization robot was made possible by National Center for Research Resources Grant 1S10RR027234-01. All experimental data were collected at the Advanced Light Source on beam 8.3.1: University of California Office of the President, Multicampus Research Programs and Initiatives Grant MR-15-328599 and the Program for Breakthrough Biomedical Research, which is partially funded by the Sandler Foundation. Molecular dynamics simulations were performed using the Temple University High-Performance Computing System Owl's Nest [purchased in part with National Science Foundation (NSF) Grant MRI-R2 0958854]. J.S.F. is a Searle Scholar and a Pew Scholar and is supported by NIH Grants OD009180 and GM110580 and by NSF Grant STC-1231306. R.A.W. is supported by a NSF Graduate Research Fellowship. We also acknowledge partial support from the NSF through Grants DMR-1120901 (to M.A.-P.) and CHE-1212416 (to G.F.).

1. Hong M, DeGrado WF (2012) Structural basis for proton conduction and inhibition by the influenza M2 protein. *Protein Sci* 21(11):1620–1633.
2. Hummer G, Rasaiah JC, Noworyta JP (2001) Water conduction through the hydrophobic channel of a carbon nanotube. *Nature* 414(6860):188–190.
3. Khademi S, et al. (2004) Mechanism of ammonia transport by Amt/MEP/Rh: Structure of AmtB at 1.35 Å. *Science* 305(5690):1587–1594.
4. Kosinska Eriksson U, et al. (2013) Subangstrom resolution X-ray structure details aquaporin-water interactions. *Science* 340(6138):1346–1349.
5. Wang C, Lamb RA, Pinto LH (1995) Activation of the M2 ion channel of influenza virus: A role for the transmembrane domain histidine residue. *Biophys J* 69(4):1363–1371.
6. Chizhmakov IV, et al. (1996) Selective proton permeability and pH regulation of the influenza virus M2 channel expressed in mouse erythroleukaemia cells. *J Physiol* 494(Pt 2):329–336.
7. Hu J, et al. (2006) Histidines, heart of the hydrogen ion channel from influenza A virus: Toward an understanding of conductance and proton selectivity. *Proc Natl Acad Sci USA* 103(18):6865–6870.
8. Stouffer AL, et al. (2008) Structural basis for the function and inhibition of an influenza virus proton channel. *Nature* 451(7178):596–599.
9. Acharya R, et al. (2010) Structure and mechanism of proton transport through the transmembrane tetrameric M2 protein bundle of the influenza A virus. *Proc Natl Acad Sci USA* 107(34):15075–15080.
10. Hu F, Schmidt-Rohr K, Hong M (2012) NMR detection of pH-dependent histidine-water proton exchange reveals the conduction mechanism of a transmembrane proton channel. *J Am Chem Soc* 134(8):3703–3713.
11. Hu F, Luo W, Hong M (2010) Mechanisms of proton conduction and gating in influenza M2 proton channels from solid-state NMR. *Science* 330(6003):505–508.
12. Sharma M, et al. (2010) Insight into the mechanism of the influenza A proton channel from a structure in a lipid bilayer. *Science* 330(6003):509–512.
13. Luo W, Hong M (2010) Conformational changes of an ion channel detected through water-protein interactions using solid-state NMR spectroscopy. *J Am Chem Soc* 132(7):2378–2384.

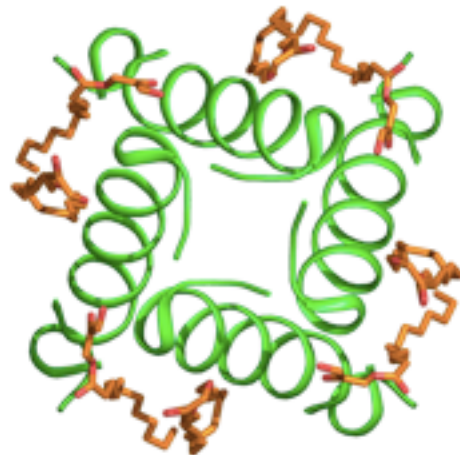
14. Carnevale V, Fiorin G, Levine BG, DeGrado WF, Klein ML (2010) Multiple proton confinement in the M2 channel from the influenza A virus. *J Phys Chem C* 114(48):20856–20863.
15. Chen H, Wu Y, Voth GA (2007) Proton transport behavior through the influenza A M2 channel: Insights from molecular simulation. *Biophys J* 93(10):3470–3479.
16. Otwinowski Z, Minor W (1997) Processing of X-ray diffraction data collected in oscillation mode. *Methods Enzymol* 276:307–326.
17. Adams PD, et al. (2010) PHENIX: A comprehensive Python-based system for macromolecular structure solution. *Acta Crystallogr D Biol Crystallogr* 66(Pt 2):213–221.
18. Wei C, Pohorille A (2013) Activation and proton transport mechanism in influenza A M2 channel. *Biophys J* 105(9):2036–2045.
19. Yi M, Cross TA, Zhou HX (2008) A secondary gate as a mechanism for inhibition of the M2 proton channel by amantadine. *J Phys Chem B* 112(27):7977–7979.
20. Ghosh A, Qiu J, DeGrado WF, Hochstrasser RM (2011) Tidal surge in the M2 proton channel, sensed by 2D IR spectroscopy. *Proc Natl Acad Sci USA* 108(15):6115–6120.
21. Schnell JR, Chou JJ (2008) Structure and mechanism of the M2 proton channel of influenza A virus. *Nature* 451(7178):591–595.
22. Wang J, et al. (2013) Structure and inhibition of the drug-resistant S31N mutant of the M2 ion channel of influenza A virus. *Proc Natl Acad Sci USA* 110(4):1315–1320.
23. Li C, Qin H, Gao FP, Cross TA (2007) Solid-state NMR characterization of conformational plasticity within the transmembrane domain of the influenza A M2 proton channel. *Biochim Biophys Acta* 1768(12):3162–3170.
24. Ma C, et al. (2009) Identification of the functional core of the influenza A virus A/M2 proton-selective ion channel. *Proc Natl Acad Sci USA* 106(30):12283–12288.
25. Landau EM, Rosenbusch JP (1996) Lipidic cubic phases: A novel concept for the crystallization of membrane proteins. *Proc Natl Acad Sci USA* 93(25):14532–14535.
26. Khurana E, et al. (2009) Molecular dynamics calculations suggest a conduction mechanism for the M2 proton channel from influenza A virus. *Proc Natl Acad Sci USA* 106(4):1069–1074.
27. Halle B (2004) Biomolecular cryocrystallography: Structural changes during flash-cooling. *Proc Natl Acad Sci USA* 101(14):4793–4798.
28. Wang J, et al. (2011) Molecular dynamics simulation directed rational design of inhibitors targeting drug-resistant mutants of influenza A virus M2. *J Am Chem Soc* 133(32):12834–12841.
29. Vangunsteren WF, Berendsen HJC, Hermans J, Hol WGJ, Postma JPM (1983) Computer-simulation of the dynamics of hydrated protein crystals and its comparison with X-ray data. *Proc Natl Acad Sci USA* 80(14):4315–4319.
30. Liu P, Huang X, Zhou R, Berne BJ (2005) Observation of a dewetting transition in the collapse of the melittin tetramer. *Nature* 437(7055):159–162.
31. Cerutti DS, Le Trong I, Stenkamp RE, Lybrand TP (2008) Simulations of a protein crystal: Explicit treatment of crystallization conditions links theory and experiment in the streptavidin-biotin complex. *Biochemistry* 47(46):12065–12077.
32. Hu Z, Jiang J (2008) Molecular dynamics simulations for water and ions in protein crystals. *Langmuir* 24(8):4215–4223.
33. Balannik V, et al. (2010) Functional studies and modeling of pore-lining residue mutants of the influenza A virus M2 ion channel. *Biochemistry* 49(4):696–708.
34. Ma C, et al. (2013) Asp44 stabilizes the Trp41 gate of the M2 proton channel of influenza A virus. *Structure* 21(11):2033–2041.
35. Liang R, Li H, Swanson JM, Voth GA (2014) Multiscale simulation reveals a multifaceted mechanism of proton permeation through the influenza A M2 proton channel. *Proc Natl Acad Sci USA* 111(26):9396–9401.
36. Dong H, Fiorin G, Degrado WF, Klein ML (2013) Exploring histidine conformations in the M2 channel lumen of the influenza A virus at neutral pH via molecular simulations. *J Phys Chem Lett* 4(18):3067–3071.
37. Caffrey M, Cherezov V (2009) Crystallizing membrane proteins using lipidic mesophases. *Nat Protoc* 4(5):706–731.
38. Fraser JS, et al. (2011) Accessing protein conformational ensembles using room-temperature X-ray crystallography. *Proc Natl Acad Sci USA* 108(39):16247–16252.
39. Tang Y, Zaitseva F, Lamb RA, Pinto LH (2002) The gate of the influenza virus M2 proton channel is formed by a single tryptophan residue. *J Biol Chem* 277(42):39880–39886.
40. Lang PT, et al. (2010) Automated electron-density sampling reveals widespread conformational polymorphism in proteins. *Protein Sci* 19(7):1420–1431.
41. Schrodinger LLC (2010) The PyMOL Molecular Graphics System, Version 1.3r1.
42. van den Bedem H, Dhanik A, Latombe JC, Deacon AM (2009) Modeling discrete heterogeneity in X-ray diffraction data by fitting multi-conformers. *Acta Crystallogr D Biol Crystallogr* 65(Pt 10):1107–1117.
43. Jorgensen WL, Chandrasekhar J, Madura JD, Impey RW, Klein ML (1983) Comparison of simple potential functions for simulating liquid water. *J Chem Phys* 79(2):926–935.
44. Phillips JC, et al. (2005) Scalable molecular dynamics with NAMD. *J Comput Chem* 26(16):1781–1802.
45. MacKerell AD, et al. (1998) All-atom empirical potential for molecular modeling and dynamics studies of proteins. *J Phys Chem B* 102(18):3586–3616.
46. Humphrey W, Dalke A, Schulter K (1996) VMD: Visual molecular dynamics. *J Mol Graph* 14(1):33–38, 27–28.
47. Best RB, et al. (2012) Optimization of the additive CHARMM all-atom protein force field targeting improved sampling of the backbone ϕ , ψ and side-chain $\chi(1)$ and $\chi(2)$ dihedral angles. *J Chem Theory Comput* 8(9):3257–3273.
48. Gianti E, Carnevale V, DeGrado WF, Klein ML, Fiorin G (2015) Hydrogen-bonded water molecules in the M2 channel of the influenza A virus guide the binding preferences of ammonium-based inhibitors. *J Phys Chem B* 119(3):1173–1183.

High resolution structures of the M2 proton channel from influenza A virus reveal dynamic pathways for proton stabilization and transduction.

Authors: Jessica L. Thomaston, Mercedes Alfonso-Prieto, Rahel A. Woldeyes, James S. Fraser, Michael L. Klein, Giacomo Fiorin, William F. DeGrado

Supplementary Information Appendix

Top-down view of the M2TM cryo high pH structure:



Side view of three M2TM tetramers within the crystal lattice:

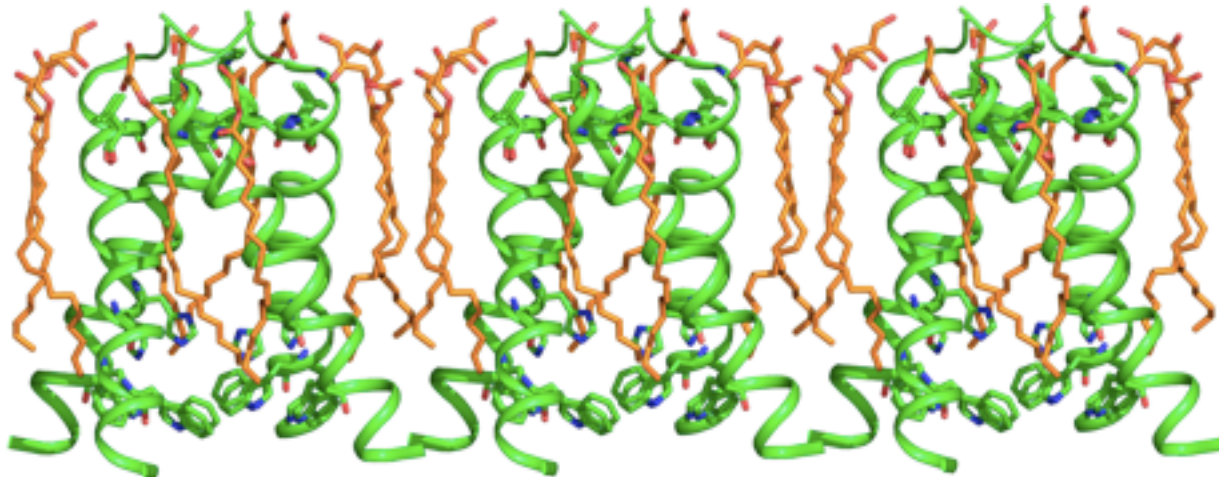


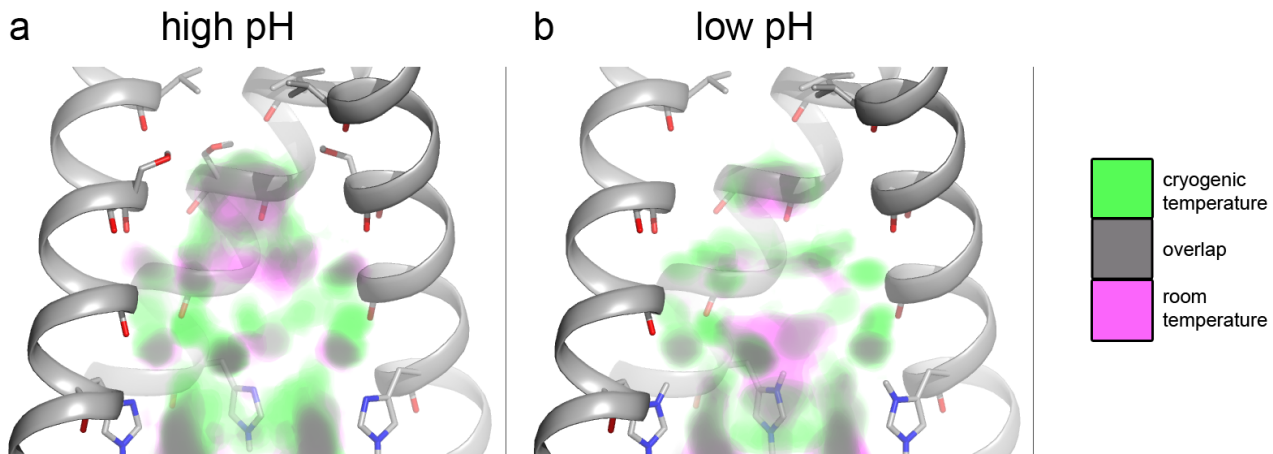
Figure S1. M2 is surrounded by monoolein molecules. The structure of the M2TM tetramer solved here using lipidic cubic phase methods is completely surrounded with monoolein molecules (orange) (see top image) at its N-terminus and shows few protein-protein contacts within the crystal lattice (see bottom image). The few protein-protein interactions that are observed take place at the C-terminus of the protein.

Data processing	cryo pH 8.0 (4QK7)	cryo pH 5.5 (4QKC)	RT pH 8.0 (4QKL)	RT pH 5.5 (4QKM)
Resolution range (Å)	13.05 - 1.1 (1.12 - 1.1)	13.06 - 1.1 (1.11 - 1.1)	20.93 - 1.711 (1.77 - 1.711)	18 - 1.44 (1.491 - 1.44)
Space group	I ₄	I ₄	I ₄	I ₄
Unit cell	29.54 29.54 66.85 90 90 90	29.31 29.3 67.31 90 90 90	29.6 29.6 68.14 90 90 90	30.09 30.09 67.39 90 90 90
Total reflections	81496(3943)	77823(3516)	5854 (622)	9117 (920)
Unique reflections	11581(575)	11596 (561)	3126 (318)	5252 (523)
Multiplicity	7.0(6.9)	6.7(6.3)	1.9 (2.0)	1.7 (1.8)
Completeness (%)	99.60 (100.00)	99.5 (66.1)	97.44 (100.00)	96.38 (97.39)
Mean I/sigma(I)	13.37 (2.8)	17.3 (3.0)	3.64 (1.65)	11.45 (1.61)
Wilson B-factor	9.19	9.19	18.65	15
R-merge	0.072(0.863)	0.050(0.544)	0.1082 (0.3675)	0.03625 (0.4499)
R-meas	0.078(0.935)	0.054(0.593)	0.153	0.05127
CC1/2	0.999(0.919)	0.999(0.934)	0.97 (0.741)	0.999 (0.798)
CC*			0.992 (0.922)	1 (0.942)

Refinement	cryo pH 8.0 (4QK7)	cryo pH 5.5 (4QKC)	RT pH 8.0 (4QKL)	RT pH 5.5 (4QKM)
Resolution range (Å)	13.05 - 1.1 (1.139 - 1.1)	13.06 - 1.1 (1.139 - 1.1)	20.93 - 1.711 (1.77 - 1.711)	18 - 1.44 (1.491 - 1.44)
R-work	0.1070 (0.1879)	0.1067 (0.1551)	0.1658 (0.2374)	0.1350 (0.1993)
R-free	0.1263 (0.1859)	0.1235 (0.1981)	0.1976 (0.2845)	0.1715 (0.2876)
Number of non-hydrogen atoms	454	458	282	323
macromolecules	356	349	244	268
ligands	62	62	11	36
water	32	42	26	18
Protein residues	27	27	27	27
RMS(bonds)	0.015	0.014	0.004	0.016
RMS(angles)	2.27	1.87	0.62	1.6
Ramachandran favored (%)	100	100	100	100
Clashscore	14.1	9.9	0	0
Average B-factor	21.3	20.7	23	28.1
macromolecules	14.6	12.5	21	19.6
ligands	47.7	48.9	29.4	80
solvent	42.1	44.3	38.2	50.6

Table S1. Crystallographic data tables. Data processing and refinement statistics for all of the M2TM structures in the main text.

Cryogenic density vs. room temp density at each pH



Molecular dynamics density vs. room temp density at each pH

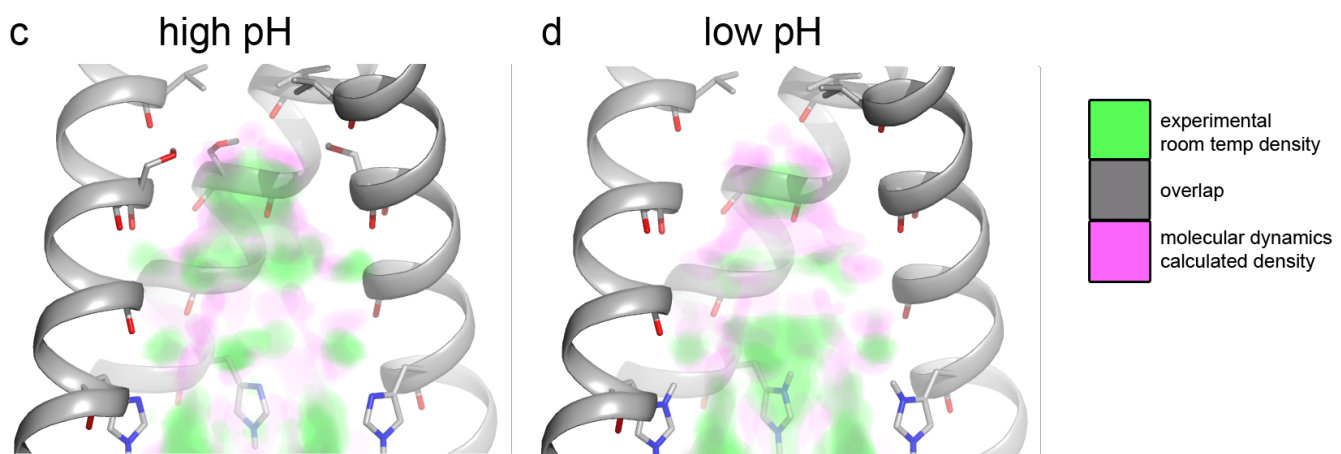


Figure S2. Further comparisons between density maps. Top, a-b: Comparison of experimentally observed density for the cryogenic and room temperature experimental conditions at high and low pH. Bottom, c-d: comparison between calculated electron density from molecular dynamics simulations and experimental density from room temperature conditions at high and low pH. The overlap between densities, shown in gray, is largest in all conditions where the waters bind to the carbonyls of the channel and also where they bind to His37.

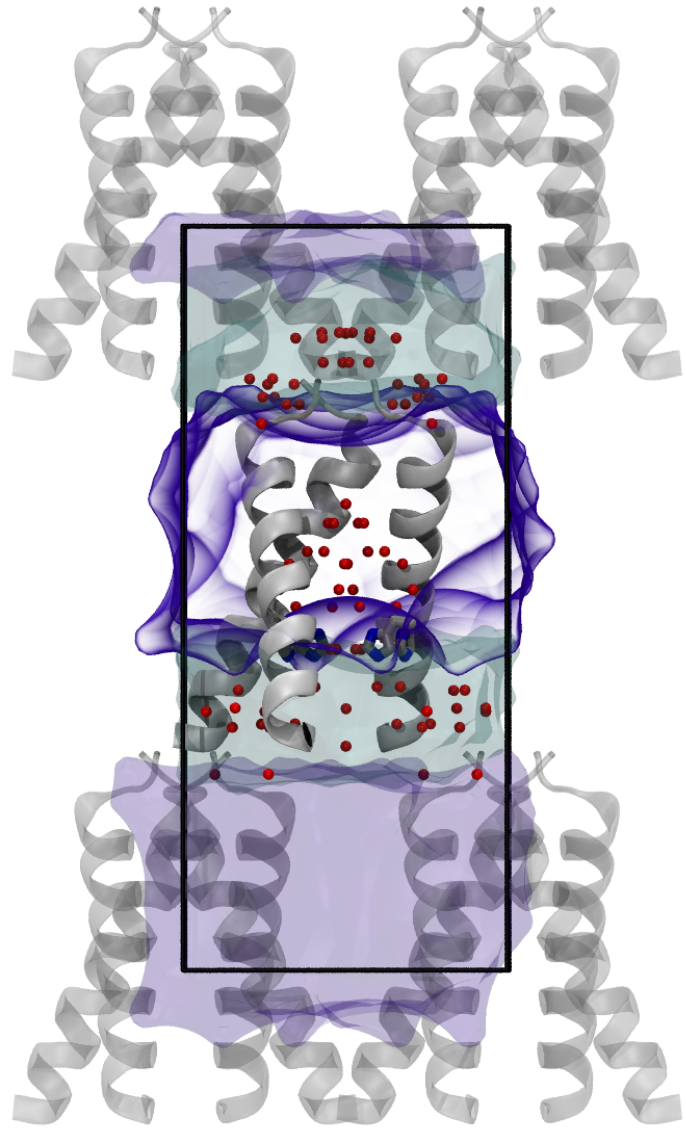


Figure S3. System setup used in the molecular dynamics simulations. The central tetramer is displayed as a grey cartoon, removing one of the helices of the tetramer in order to show the crystallographic water molecules and the His37 tetrad. The rest of the water is shown in cyan and the lipidic phase in purple. The simulation box is indicated with black lines, and contains an additional staggered tetramer in order to model the I₄ crystallographic symmetry.

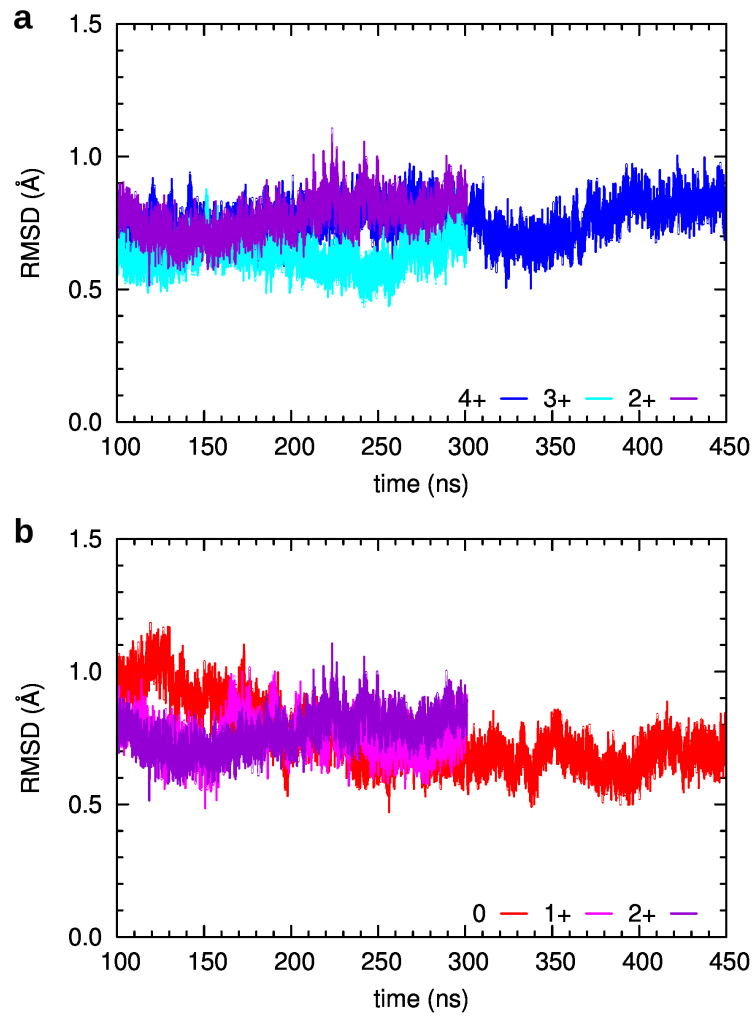


Figure S4. Evolution of the root mean square deviation (RMSD) of the Ca atoms of M2TM along the MD simulations. RMSD is calculated with respect to the cryogenic crystal structures. **a**, RMSD for the 4+ (blue), 3+ (cyan) and 2+ (purple) states with respect to the low pH structure (PDB entry 4QKC). **b**, RMSD for neutral (red), 1+ (magenta) and 2+ (purple) states with respect to the high pH structure (PDB entry 4QK7).

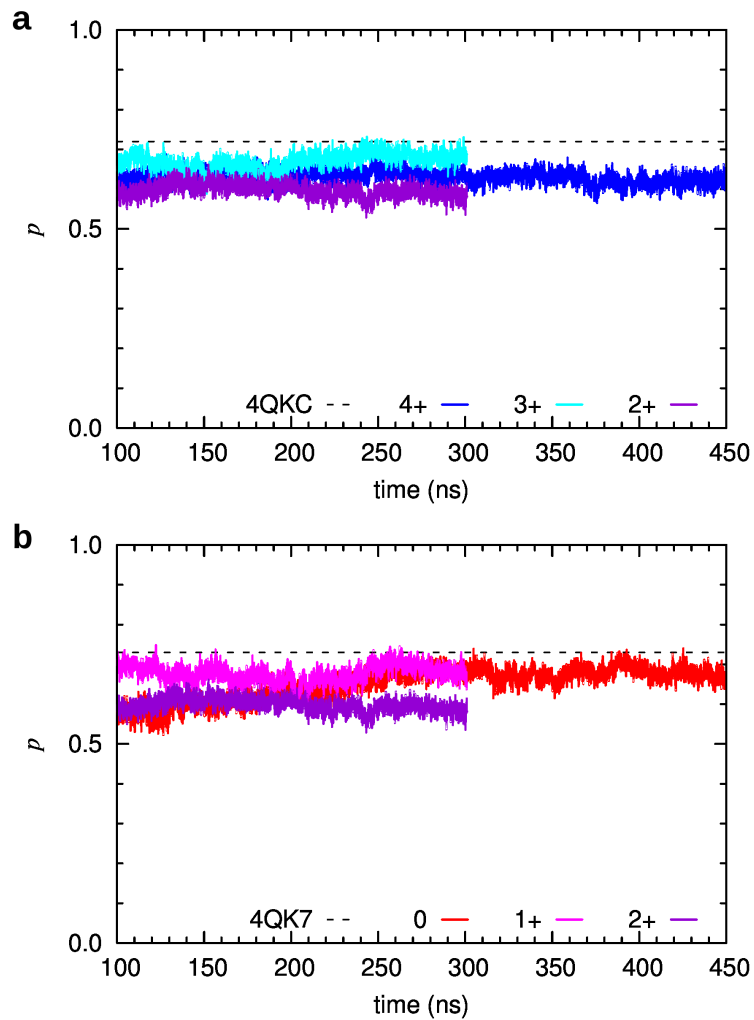


Figure S5. Evolution of the principal component, p , along the MD simulations. p describes the fraction of C-terminally closed *versus* dilated protein conformation. **a**, Principal component for the 4+ (blue), 3+ (cyan) and 2+ (purple) states; the principal component of the cryogenic crystal structure at low pH (PDB entry 4QKC) is shown as a black dashed line. **b**, Principal component for the neutral (red), 1+ (magenta) and 2+ (purple) states; the principal component of the cryogenic crystal structure at high pH (PDB entry 4QK7) is shown as a black dashed line.

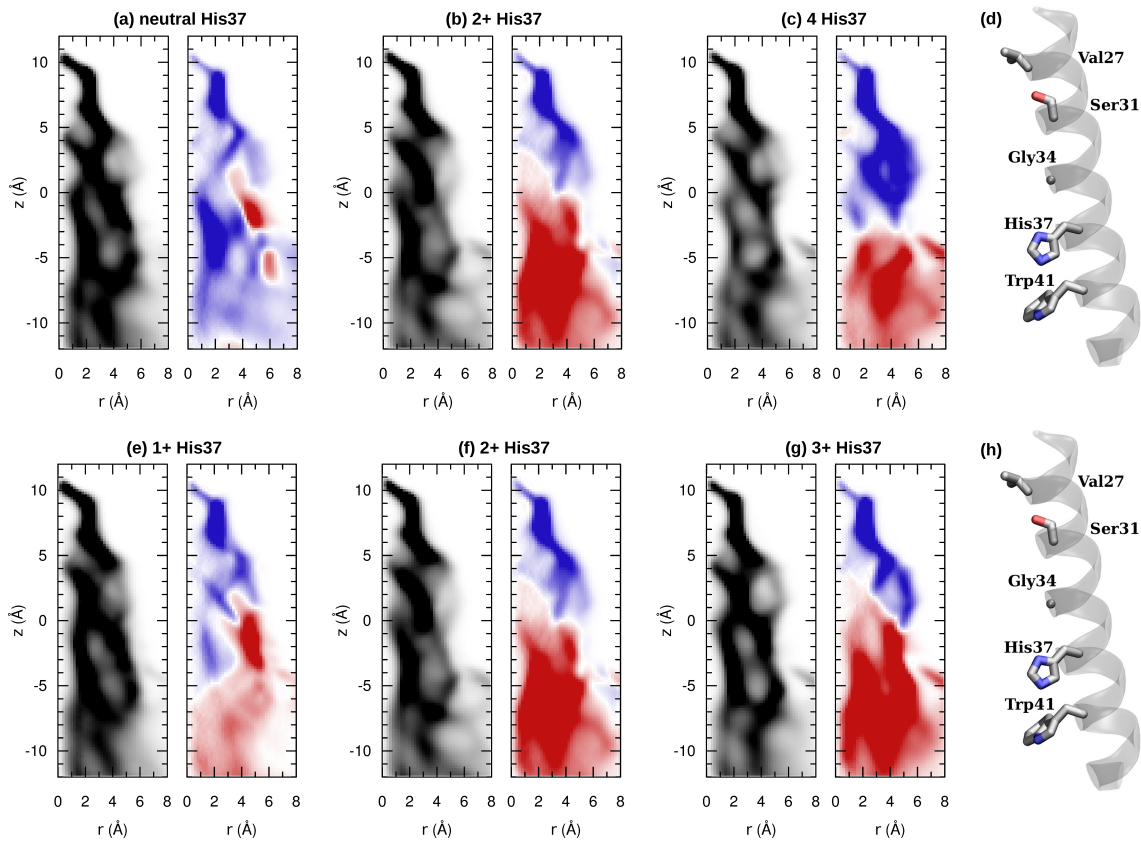


Figure S6. Two-dimensional profile of the hydrogen bond vectors at different charge states of the His37 tetrad. Shown are the density (black, \AA^{-3} units) and average orientation (red and blue, \AA^{-2} units) of hydrogen bond vectors as a function of the distance from the pore axis, r , and the displacement along the axis, z . Blue areas indicate regions populated by outward-oriented H-bonds, red denote inward-oriented H-bonds. *Top:* **a-c**, Density and average orientation of hydrogen bond vectors for a neutral channel, at the 2+ charge state and at the 4+ charge state, respectively. **d**, M2TM monomer, indicating the position of the pore-lining residues (Val27, Ser31, His37 and Trp41). *Bottom:* **e-g**, Density and average orientation of hydrogen bond vectors at the 1+, 2+ and the 3+ charge states, respectively; the 2+ charge state is the same as in (b). **h**, M2TM monomer, indicating the position of the pore-lining residues (Val27, Ser31, His37 and Trp41).

Table S2. Average number of hydrogen bonds in the M2 pore at different charge states of the His37 tetrad. The hydrogen bonds are classified as extraviral or intraviral depending on their position (either above or below) with respect to the His37 tetrad. The total number of hydrogen bonds is decomposed in outwards (in blue) or inwards (in red) depending on the hydrogen bond orientation (either towards the viral exterior or interior, respectively).

		neutral His37	2+ His37	4+ His37
extraviral (above His37)	total	41.8 ± 4.8	37.7 ± 4.3	33.3 ± 4.2
	outwards	22.4 ± 3.7	22.1 ± 3.6	20.7 ± 4.0
	inwards	19.5 ± 3.6	15.6 ± 3.4	12.6 ± 3.8
intraviral (below His37)	total	53.8 ± 6.2	38.0 ± 5.8	46.3 ± 6.2
	outwards	29.8 ± 5.0	13.8 ± 3.9	16.9 ± 4.9
	inwards	24.0 ± 4.7	24.2 ± 4.9	29.4 ± 5.6

		1+ His37	2+ His37	3+ His37
extraviral (above His37)	total	41.2 ± 4.7	37.7 ± 4.3	40.5 ± 4.4
	outwards	20.5 ± 3.6	22.1 ± 3.6	20.1 ± 3.5
	inwards	20.8 ± 3.6	15.6 ± 3.4	20.4 ± 3.5
intraviral (below His37)	total	49.7 ± 5.8	38.0 ± 5.8	48.9 ± 6.6
	outwards	22.5 ± 4.3	13.8 ± 3.9	13.4 ± 4.0
	inwards	27.2 ± 4.9	24.2 ± 4.9	35.5 ± 5.8

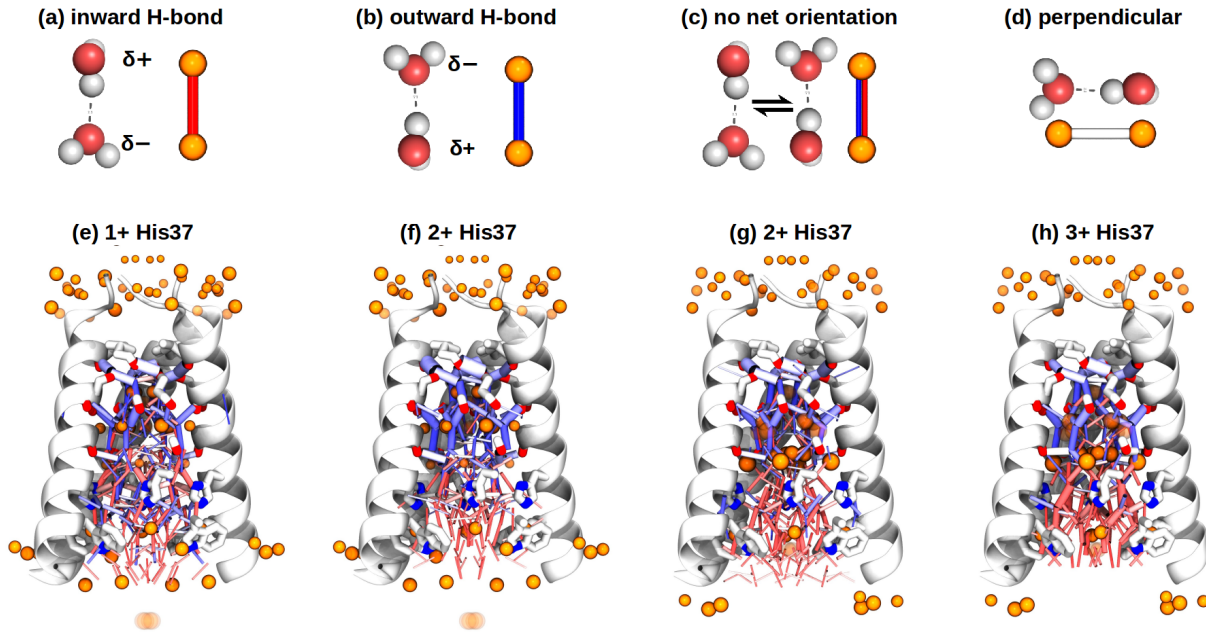


Figure S7. Water wires calculated from the molecular dynamics simulations at different charge states of the His37 tetrad. *Top*, Schematic representation of the four possible hydrogen bond patterns between water molecules inside the M2 pore. **a-b**, Directional hydrogen bonds oriented towards either the viral interior (a) or the channel exterior (b), respectively. **c**, Hydrogen bond without a preferred directionality (*i.e.* flips back and forth between the two orientations). **d**, Hydrogen bond perpendicular to the pore axis. For each possible hydrogen bond pattern, the atomistic representation of the corresponding water dimer is shown on the left and the water wire counterpart on the right, with the water oxygen atoms as orange spheres and the hydrogen bonds as sticks; the color scale denotes the hydrogen bond orientation, either inwards (in red), outwards (in blue) or perpendicular to the pore axis (in white). *Bottom*, Water wires calculated from the MD simulations. The oxygen atoms of the water molecules observed in the room temperature X-ray structures are shown as van der Waals spheres (orange color), with the diameter proportional to the crystallographic B-factors and transparency reflecting partial occupancy. Hydrogen bonds are represented as sticks, with a color scale denoting their orientation (see panels a-d), and thickness proportional to their population. **e-f**, Water wires for the 1+ and 2+ charge states, respectively, for the production simulations starting from the cryogenic high pH crystal structure (PDB entry 4QK7). **g-h**, Water wires at the 2+ and 3+ charge states, respectively, for the production simulations starting from the cryogenic low pH crystal structure (PDB entry 4QKC).

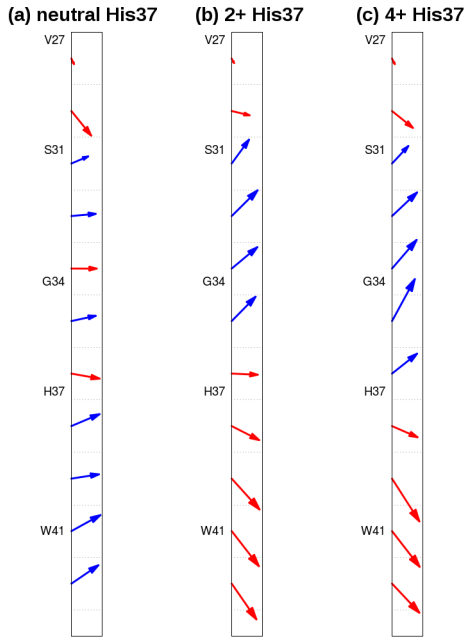
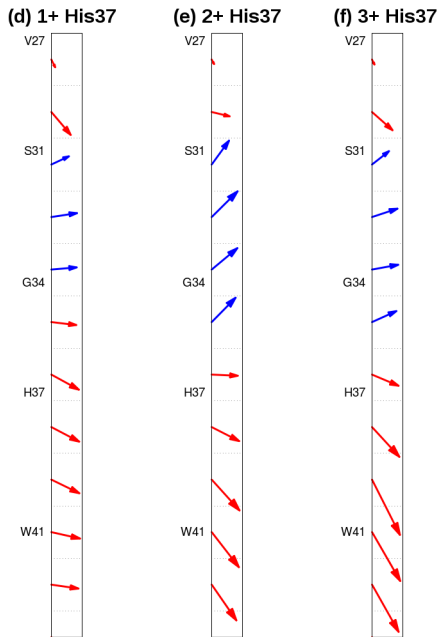


Figure S8. Average hydrogen bond vectors along the M2 pore at different charge states of the His37 tetrad. The vector direction reflects the net orientation with respect to the pore axis, with the H-bonds pointing to the exterior of the channel (outwards) colored in blue and the ones pointing to the viral interior (inwards) in red. The vector length is proportional to the magnitude of the net hydrogen bond (i.e. the longer, the larger the preference to be oriented in that direction). The hydrogen bonds are averaged over 2 Å bins along the pore axis (delimited by dashed black lines). **a-c**, Average hydrogen bond vectors for a neutral channel, at the 2+ charge state and at the 4+ charge state, respectively. **d-f**, Average hydrogen bond vectors at the 1+, 2+ and 3+ charge states, respectively.



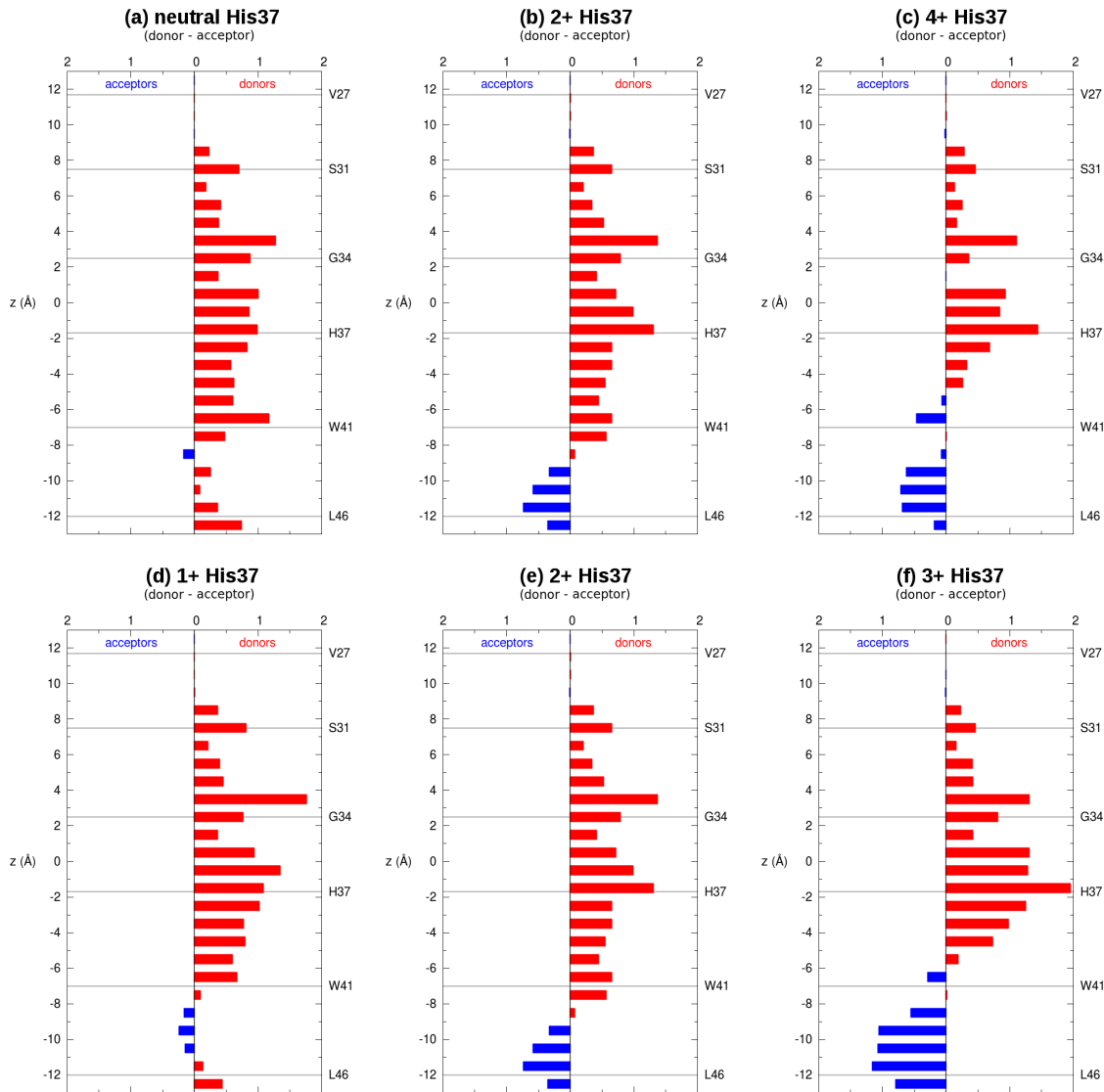


Figure S9. Difference between the number of water molecules acting as hydrogen bond donors and acceptors at different charge states of the His37 tetrad. The (donor–acceptor) difference along the M2 pore axis (z , in Å) is shown. Red bars represent a net number of donors at that pore position and blue bars a net number of acceptors. The position of the pore-lining M2 residues (C_{α} atom of Val27, Ser31, Gly34, His37, Trp41 and Leu46) is indicated by horizontal grey lines. **a-c**, Difference (donor–acceptor) for a neutral channel, at the 2+ charge state and at the 4+ charge state, respectively. **d-f**, Difference (donor–acceptor) at the 1+, 2+ and 3+ charge states; the 2+ state is the same as in **b**.

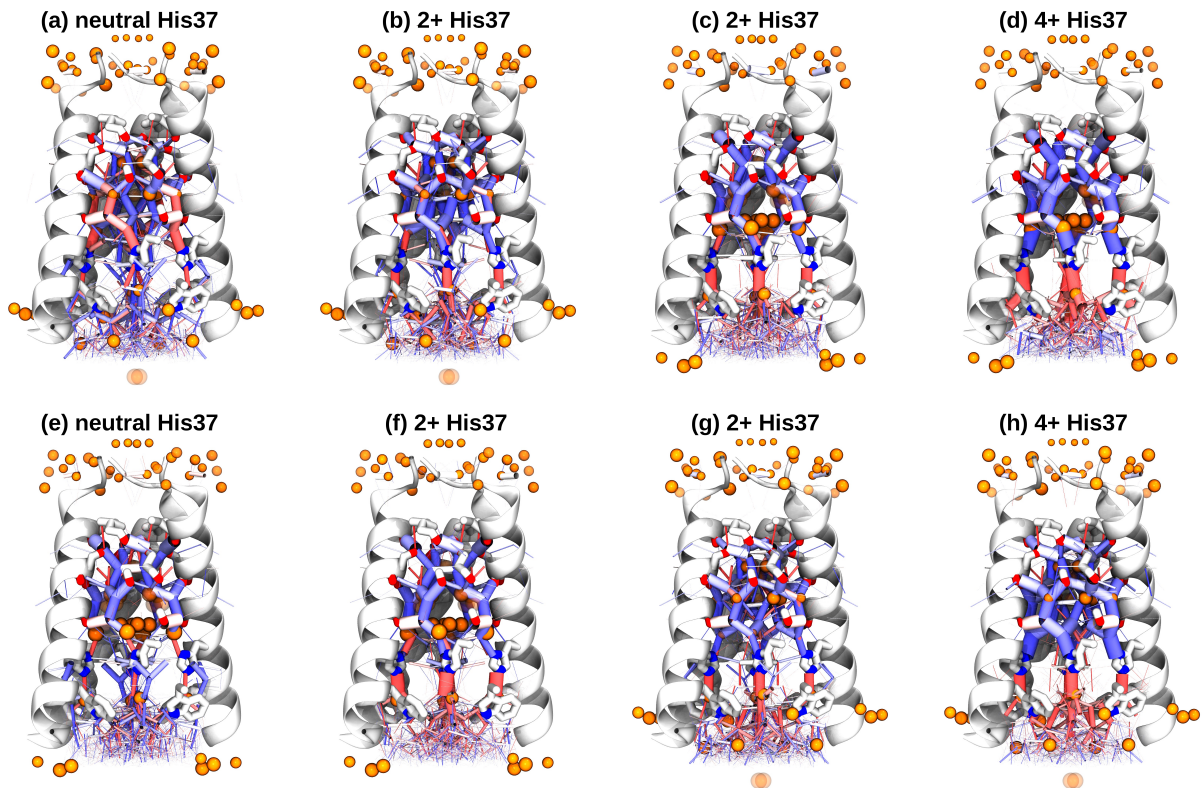


Figure S10. Water wires calculated from the control simulations at different charge states of the His37 tetrad. The oxygen atoms of the water molecules observed in the room temperature X-ray structures are shown as van der Waals spheres (orange color), with the diameter proportional to the crystallographic B-factors and transparency reflecting partial occupancy. Hydrogen bonds are represented as sticks, with a color scale denoting their orientation (see Supplementary Figure S7), and thickness proportional to their population. *Top*, Restrained MD simulations. **a-b**, Water wires for the neutral charge state and at the 2+ charge state, respectively, for the restrained simulations starting from the high pH crystal structure (PDB entry 4QK7). **c-d**, Water wires at the 2+ and 4+ charge states, respectively, for the restrained simulations starting from the low pH crystal structure (PDB entry 4QKC). *Bottom*, Swapped MD simulations. **e-f**, Water wires for the neutral charge state and at the 2+ charge state, respectively, for the swapped simulations with the high pH protein structure and low pH water sites. **g-h**, Water wires at the 2+ and 4+ charge states, respectively, for the swapped simulations with the low pH protein structure and high pH water sites.

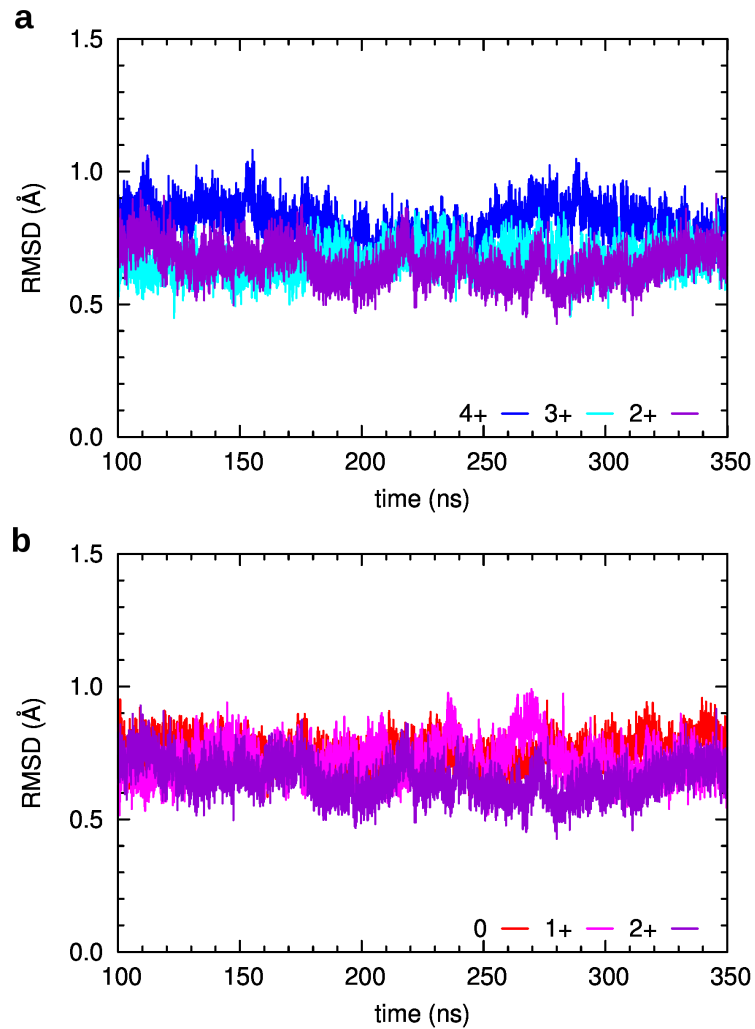


Figure S11. Evolution of the root mean square deviation (RMSD) of the Ca atoms of M2TM along the MD simulations of the S31N mutant. RMSD is calculated with respect to the cryogenic crystal structures. **a**, RMSD for the 4+ (blue), 3+ (cyan) and 2+ (purple) states with respect to the low pH structure (PDB entry 4QKC). **b**, RMSD for neutral (red), 1+ (magenta) and 2+ (purple) states with respect to the high pH structure (PDB entry 4QK7).

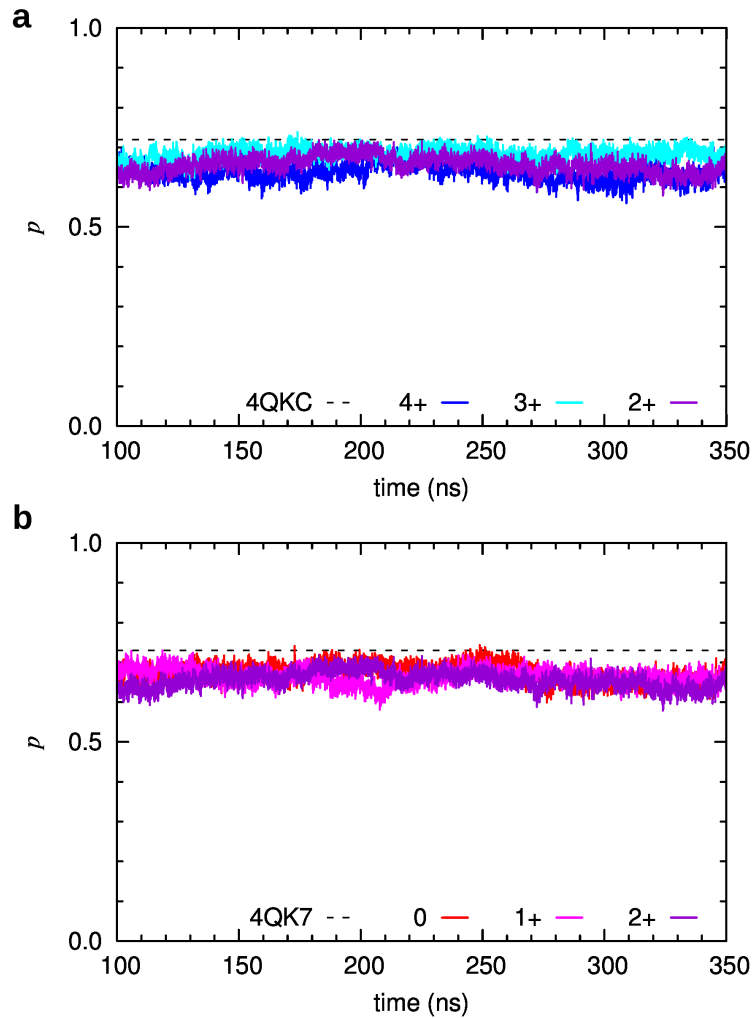


Figure S12. Evolution of the principal component, p , along the MD simulations of the S31N M2TM mutant. p describes the fraction of C-terminally closed *versus* dilated protein conformation. **a**, Principal component for the 4+ (blue), 3+ (cyan) and 2+ (purple) states; the principal component of the cryogenic crystal structure at low pH (PDB entry 4QKC) is shown as a black dashed line. **b**, Principal component for the neutral (red), 1+ (magenta) and 2+ (purple) states; the principal component of the cryogenic crystal structure at high pH (PDB entry 4QK7) is shown as a black dashed line.

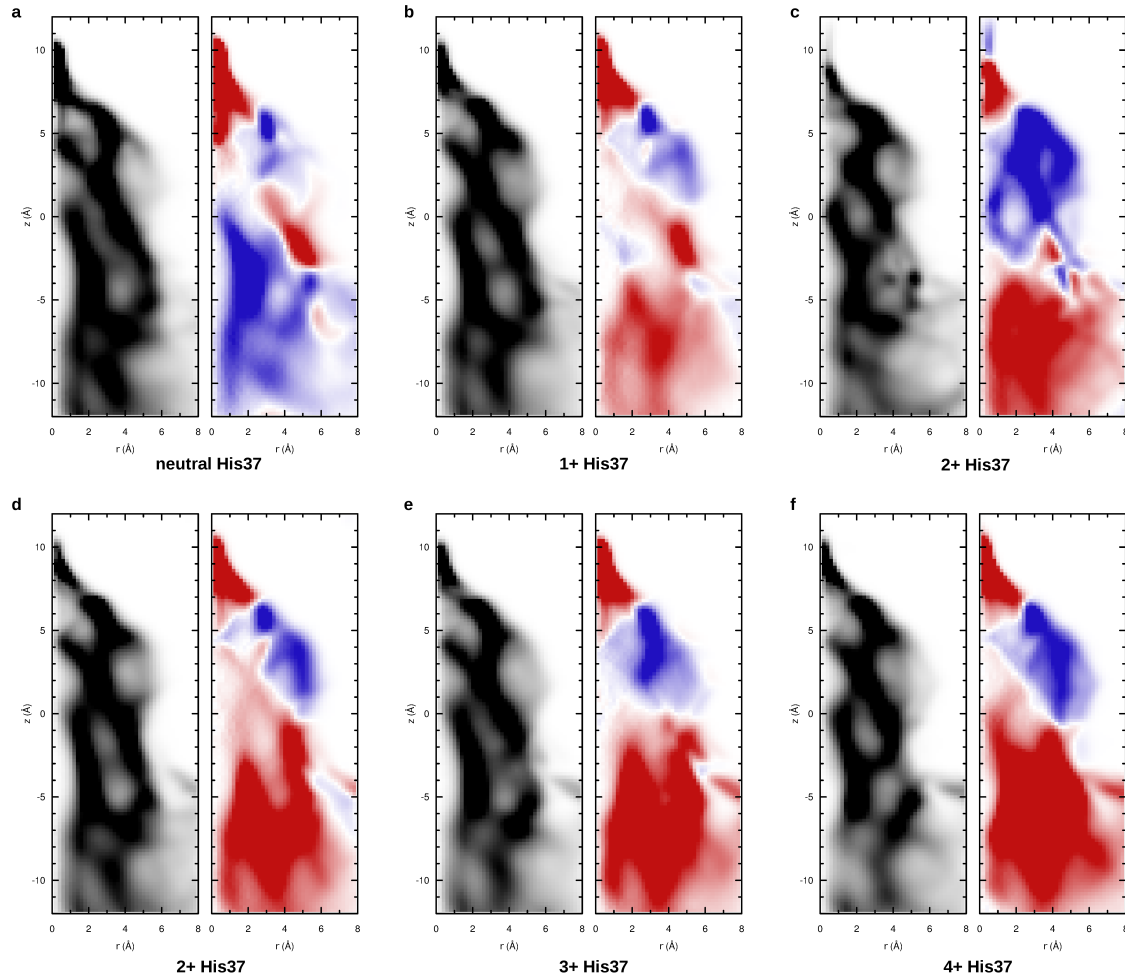


Figure S13. Two-dimensional profile of the hydrogen bond vectors at different charge states of the His37 tetrad for the S31N mutant. Shown are the density (black, \AA^{-3} units) and average orientation (red and blue, \AA^{-2} units) of hydrogen bond vectors as a function of the distance from the pore axis, r , and the displacement along the axis, z . Blue areas indicate regions populated by outward-oriented H-bonds, red denote inward-oriented H-bonds. *Top:* **a-c**, Density and average orientation of hydrogen bond vectors at the 0, 1+, 2+ charge states, respectively, started from the high pH cryo structure. *Bottom:* **d-f**, Density and average orientation of hydrogen bond vectors for at the 2+, 3+ and 4+ charge states, respectively, started from the low pH cryo structure.

Table S3. Average number of hydrogen bonds in the M2 pore at different charge states of the His37 tetrad for the S31N M2 mutant. The hydrogen bonds are classified as extraviral or intraviral depending on their position (either above or below) with respect to the His37 tetrad. The total number of hydrogen bonds is decomposed in outwards (in blue) or inwards (in red) depending on the hydrogen bond orientation (either towards the viral exterior or interior, respectively). The 4QK7-based simulations were started from the low pH cryogenic X-ray structure and the 4QKC-based from the high pH cryogenic X-ray structure.

4QK7-based simulations		neutral His37	1+ His37	2+ His37
extraviral (above His37)	total	38.1 ± 4.8	39.9 ± 5.0	31.1 ± 4.1
	outwards	18.9 ± 3.6	18.9 ± 3.5	18.4 ± 3.3
	inwards	19.4 ± 3.5	21.0 ± 3.9	12.7 ± 3.0
	total	52.5 ± 6.2	52.0 ± 6.5	46.5 ± 5.9
	outwards	30.1 ± 5.1	22.8 ± 4.7	17.9 ± 4.2
	inwards	22.4 ± 4.5	29.2 ± 5.3	28.6 ± 5.1
4QKC-based simulations		2+ His37	3+ His37	4+ His37
extraviral (above His37)	total	39.5 ± 4.5	38.3 ± 4.4	35.7 ± 4.2
	outwards	18.8 ± 3.4	18.1 ± 3.3	17.3 ± 3.1
	inwards	20.7 ± 3.5	20.2 ± 3.5	18.4 ± 3.4
	total	53.2 ± 6.6	48.6 ± 5.6	45.7 ± 5.7
	outwards	18.9 ± 4.4	14.1 ± 3.8	10.1 ± 3.4
	inwards	34.2 ± 5.6	34.5 ± 5.3	35.6 ± 5.4

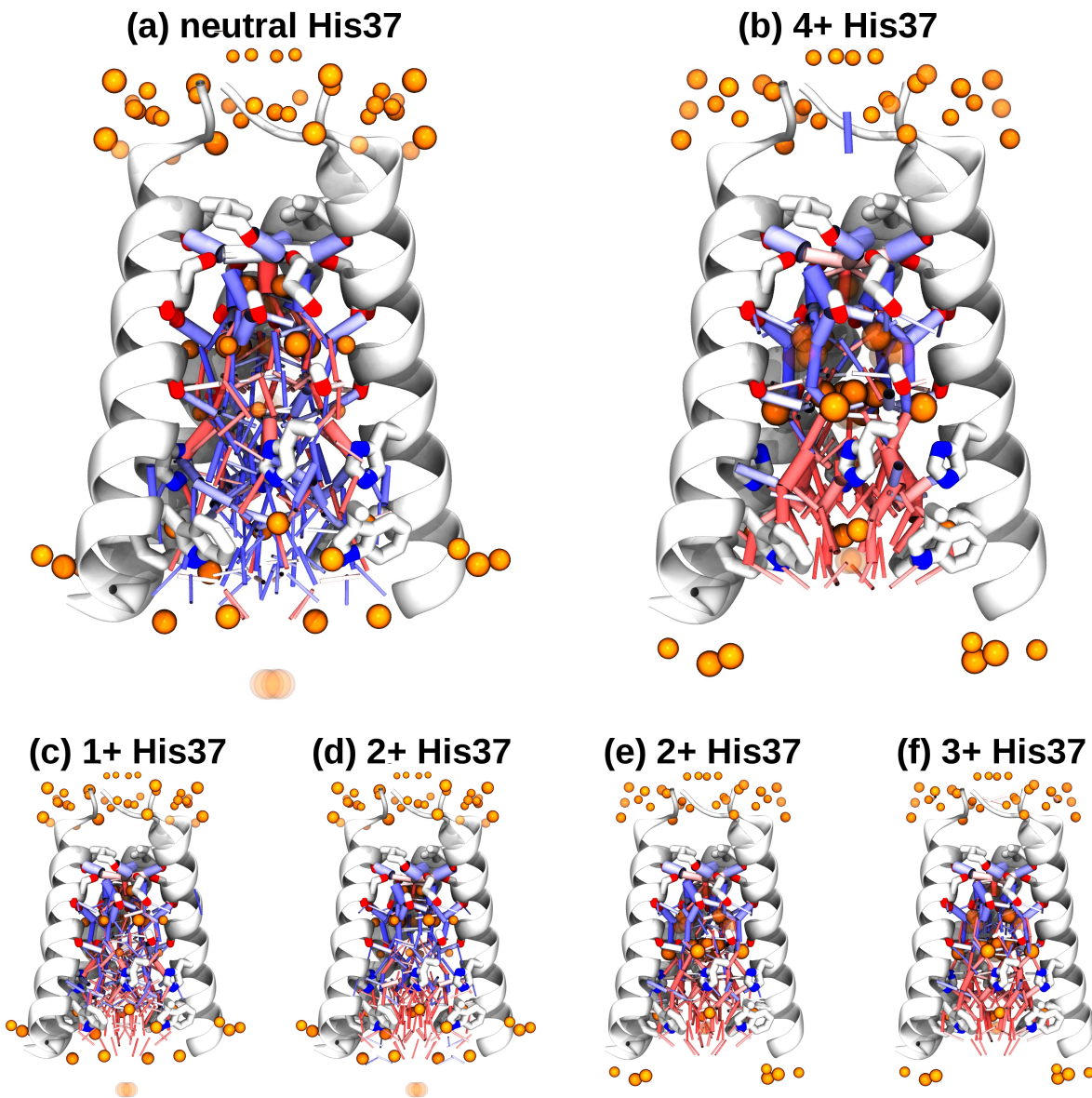


Figure S14. Water wires calculated from the molecular dynamics simulations at different charge states of the His37 tetrad for the S31N mutant. The oxygen atoms of the water molecules observed in the room temperature X-ray structures are shown as orange van der Waals spheres (orange color), with the diameter proportional to the crystallographic B-factors and transparency reflecting partial occupancy. Hydrogen bonds are represented as sticks, with a color scale denoting their orientation (see panels a-d), and thickness proportional to their population. **a** and **c-d**, Water wires for the 0, 1+ and 2+ charge states, respectively, for the production simulations starting from the cryogenic high pH crystal structure (PDB entry 4QK7). **b** and **d-e**, Water wires at the 4+, 2+ and 3+ charge states, respectively, for the production simulations starting from the cryogenic low pH crystal structure (PDB entry 4QKC). N.B.: the water wires of the S31N simulation are shown over the room temperature structure of wild-type M2TM, thus the residue displayed at position 31 is a serine instead of the asparagine used in the simulation.

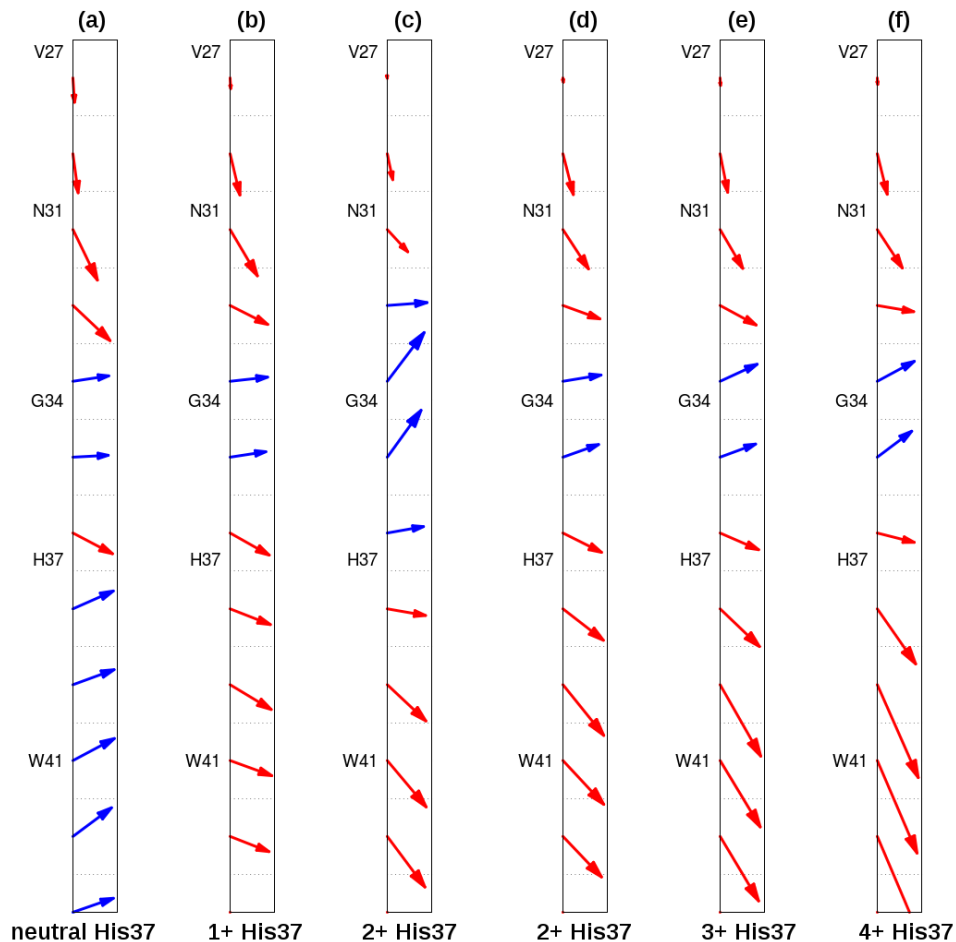


Figure S15. Average hydrogen bond vectors along the M2 pore at different charge states of the His37 tetrad for the S31N mutant. The vector direction reflects the net orientation with respect to the pore axis, with the H-bonds pointing to the exterior of the channel (outwards) colored in blue and the ones pointing to the viral interior (inwards) in red. The vector length is proportional to the magnitude of the net hydrogen bond (i.e. the longer, the larger the preference to be oriented in that direction). The hydrogen bonds are averaged over 2 Å bins along the pore axis (delimited by dashed black lines). **a-c**, Average hydrogen bond vectors at the 0, 1+, 2+ charge states, respectively, for the production simulations starting from the high pH cryogenic crystal structure (PDB entry 4QK7). **d-f**, Average hydrogen bond vectors at the 2+, 3+, 4+ charge states, respectively, for the production simulations starting from the low pH cryogenic crystal structure (PDB entry 4QKC).

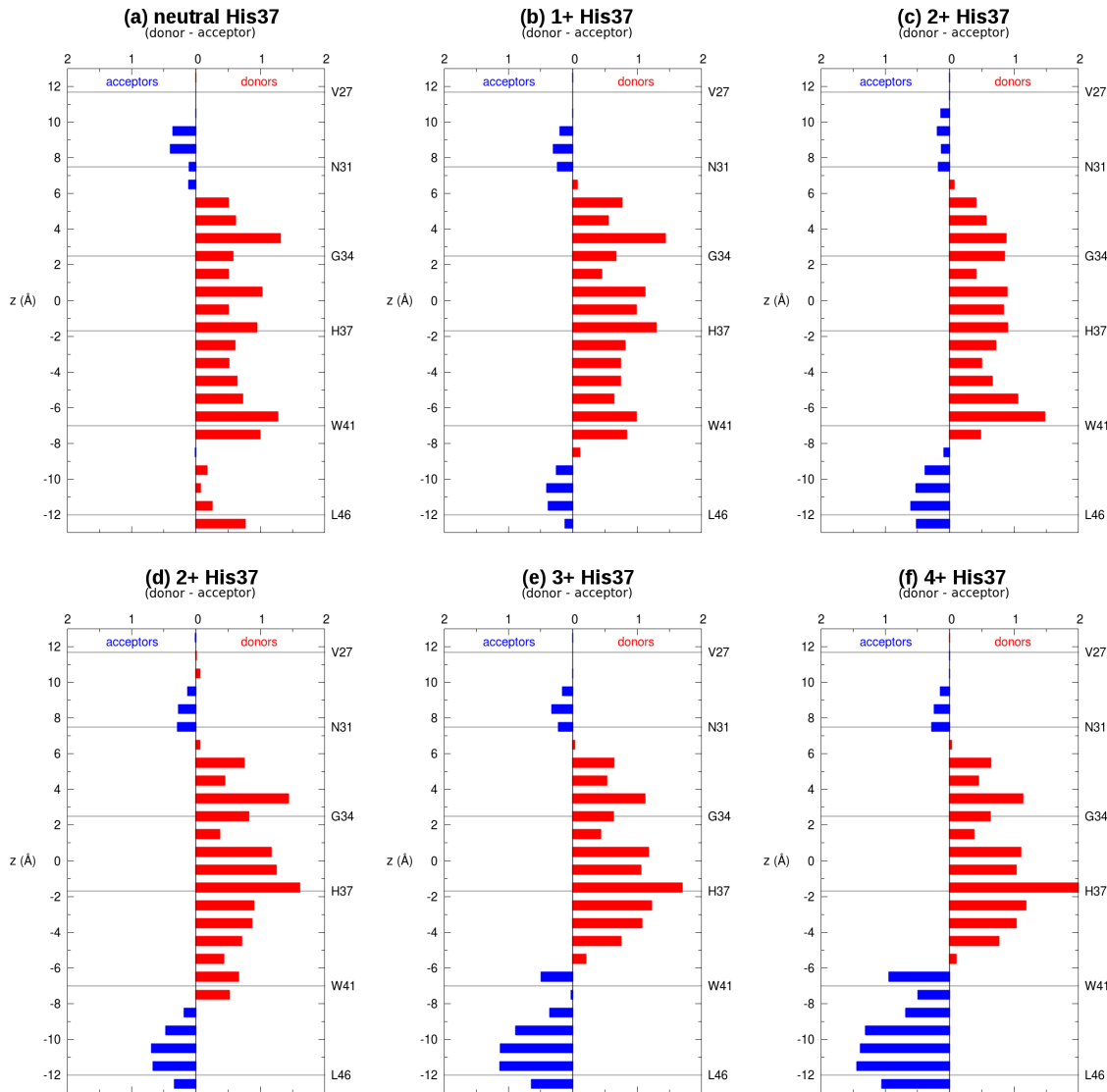


Figure S16. Difference between the number of water molecules acting as hydrogen bond donors and acceptors at different charge states of the His37 tetrad for the S31N mutant. The (*donor–acceptor*) difference along the M2 pore axis (z , in Å) is shown. Red bars represent a net number of donors at that pore position and blue bars a net number of acceptors. The position of the pore-lining M2 residues (C_α atom of Val27, Ser31, Gly34, His37, Trp41 and Leu46) is indicated by horizontal grey lines. **a-c**, Difference (*donor–acceptor*) at the 0, 1+ and 2+ charge states, respectively, for the production simulations starting from the cryogenic high pH crystal structure (PDB entry 4QK7). **d-f**, Difference (*donor–acceptor*) at the 2+, 3+ and 4+ charge states, respectively, for the production simulations starting from the cryogenic low pH crystal structure (PDB entry 4QKC).

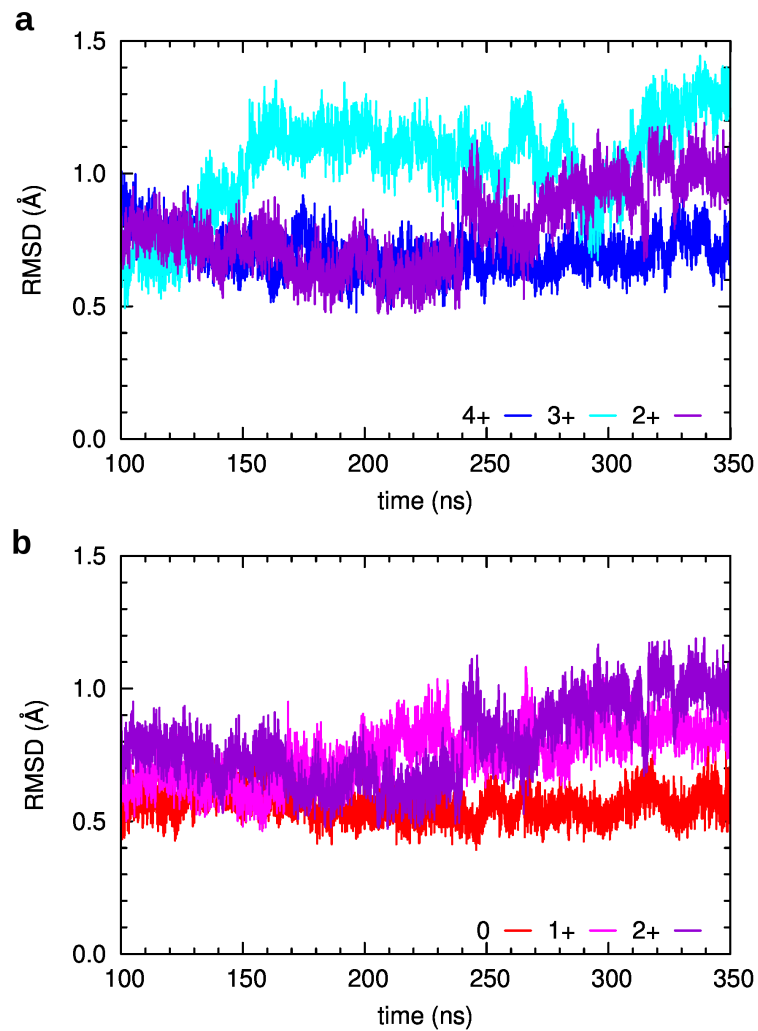


Figure S17. Evolution of the root mean square deviation (RMSD) of the Ca atoms of M2TM along the MD simulations of the D44N mutant. RMSD is calculated with respect to the cryogenic crystal structures. **a**, RMSD for the 4+ (blue), 3+ (cyan) and 2+ (purple) states with respect to the low pH structure (PDB entry 4QKC). **b**, RMSD for neutral (red), 1+ (magenta) and 2+ (purple) states with respect to the high pH structure (PDB entry 4QK7).

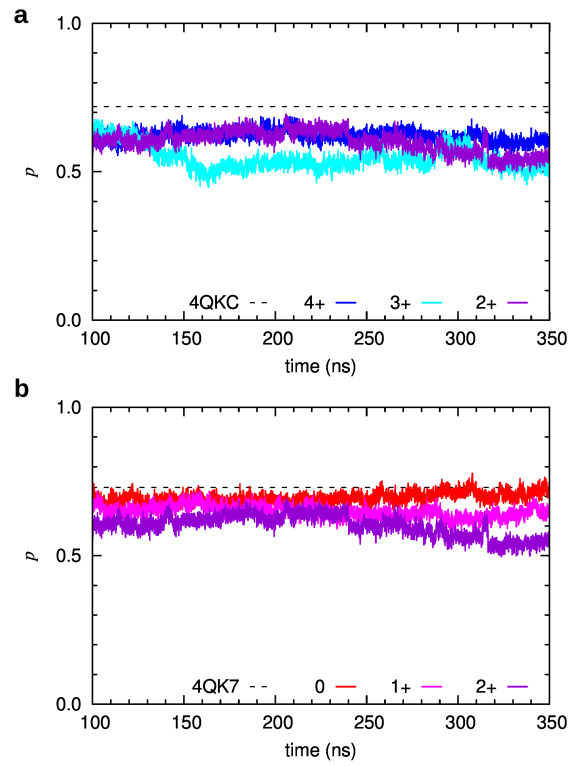


Figure S18. Evolution of the principal component, p , along the MD simulations of the D44N M2TM mutant. p describes the fraction of C-terminally closed *versus* dilated protein conformation. **a**, Principal component for the 4+ (blue), 3+ (cyan) and 2+ (purple) states; the principal component of the cryogenic crystal structure at low pH (PDB entry 4QKC) is shown as a black dashed line. **b**, Principal component for the neutral (red), 1+ (magenta) and 2+ (purple) states; the principal component of the cryogenic crystal structure at high pH (PDB entry 4QK7) is shown as a black dashed line.

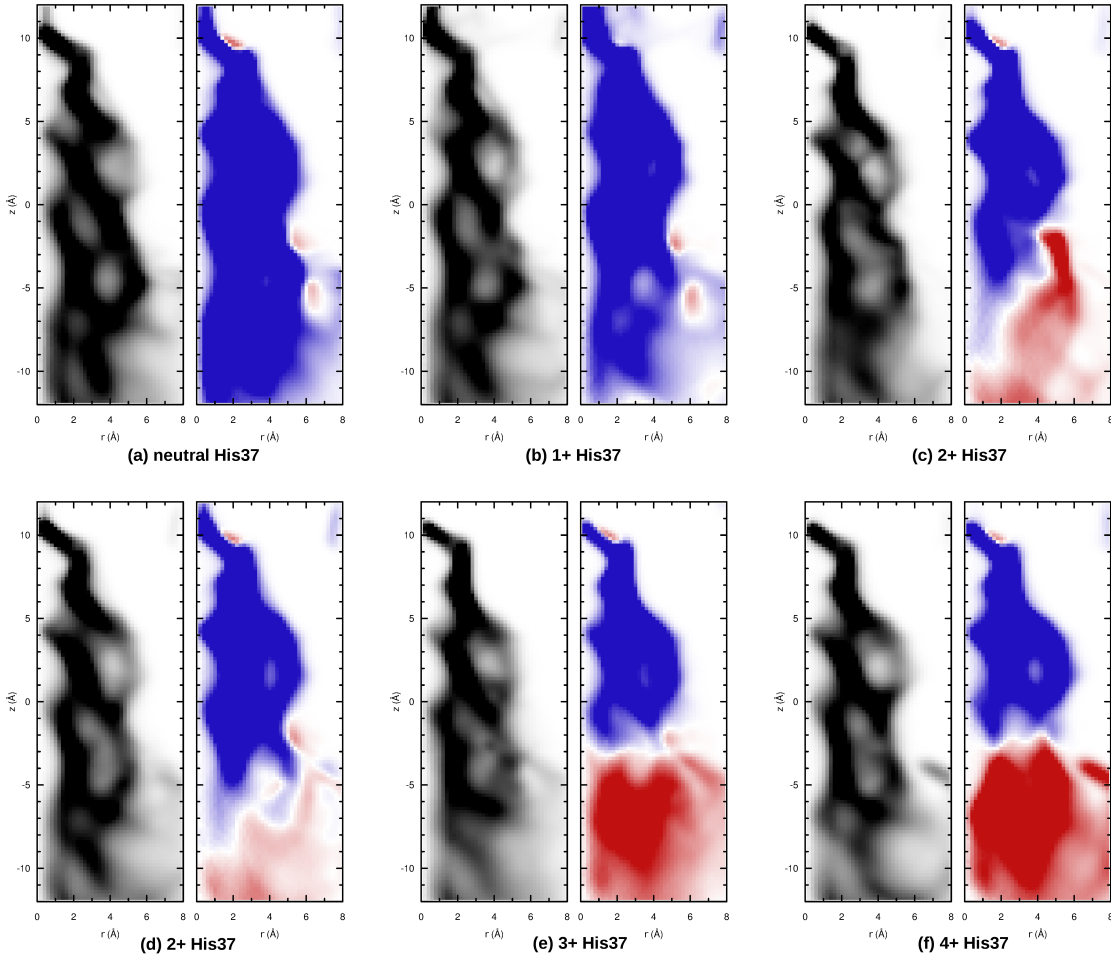


Figure S19. Two-dimensional profile of the hydrogen bond vectors at different charge states of the His37 tetrad for the D44N mutant. Shown are the density (black, \AA^{-3} units) and average orientation (red and blue, \AA^{-2} units) of hydrogen bond vectors as a function of the distance from the pore axis, r , and the displacement along the axis, z . Blue areas indicate regions populated by outward-oriented H-bonds, red denote inward-oriented H-bonds. *Top:* **a-c**, Density and average orientation of hydrogen bond vectors at the 0, 1+, 2+ charge states, respectively, started from the high pH cryo structure. *Bottom:* **d-f**, Density and average orientation of hydrogen bond vectors for at the 2+, 3+ and 4+ charge states, respectively, started from the low pH cryo structure.

Table S4. Average number of hydrogen bonds in the M2 pore at different charge states of the His37 tetrad for the D44N M2 mutant. The hydrogen bonds are classified as extraviral or intraviral depending on their position (either above or below) with respect to the His37 tetrad. The total number of hydrogen bonds is decomposed in outwards (in blue) or inwards (in red) depending on the hydrogen bond orientation (either towards the viral exterior or interior, respectively).

4QK7-based simulations		neutral His37	1+ His37	2+ His37
extraviral (above His37)	total	45.9 ± 4.9	41.6 ± 5.5	37.1 ± 4.5
	outwards	36.5 ± 4.4	34.1 ± 4.5	27.2 ± 4.0
	inwards	9.4 ± 2.8	7.6 ± 2.9	9.8 ± 2.7
intraviral (below His37)	total	51.9 ± 6.3	45.4 ± 6.7	42.1 ± 6.4
	outwards	38.2 ± 5.2	27.3 ± 5.2	18.4 ± 4.5
	inwards	13.7 ± 3.7	18.1 ± 4.1	23.7 ± 4.5
4QKC-based simulations		2+ His37	3+ His37	4+ His37
extraviral (above His37)	total	40.5 ± 4.5	38.3 ± 4.6	40.5 ± 4.5
	outwards	31.4 ± 4.1	26.6 ± 4.0	28.3 ± 4.0
	inwards	9.1 ± 2.7	11.7 ± 3.0	12.2 ± 3.0
intraviral (below His37)	total	48.1 ± 5.9	42.4 ± 6.0	49.0 ± 6.1
	outwards	23.5 ± 4.3	14.5 ± 4.0	13.1 ± 3.8
	inwards	24.6 ± 4.9	27.8 ± 5.2	35.9 ± 5.7

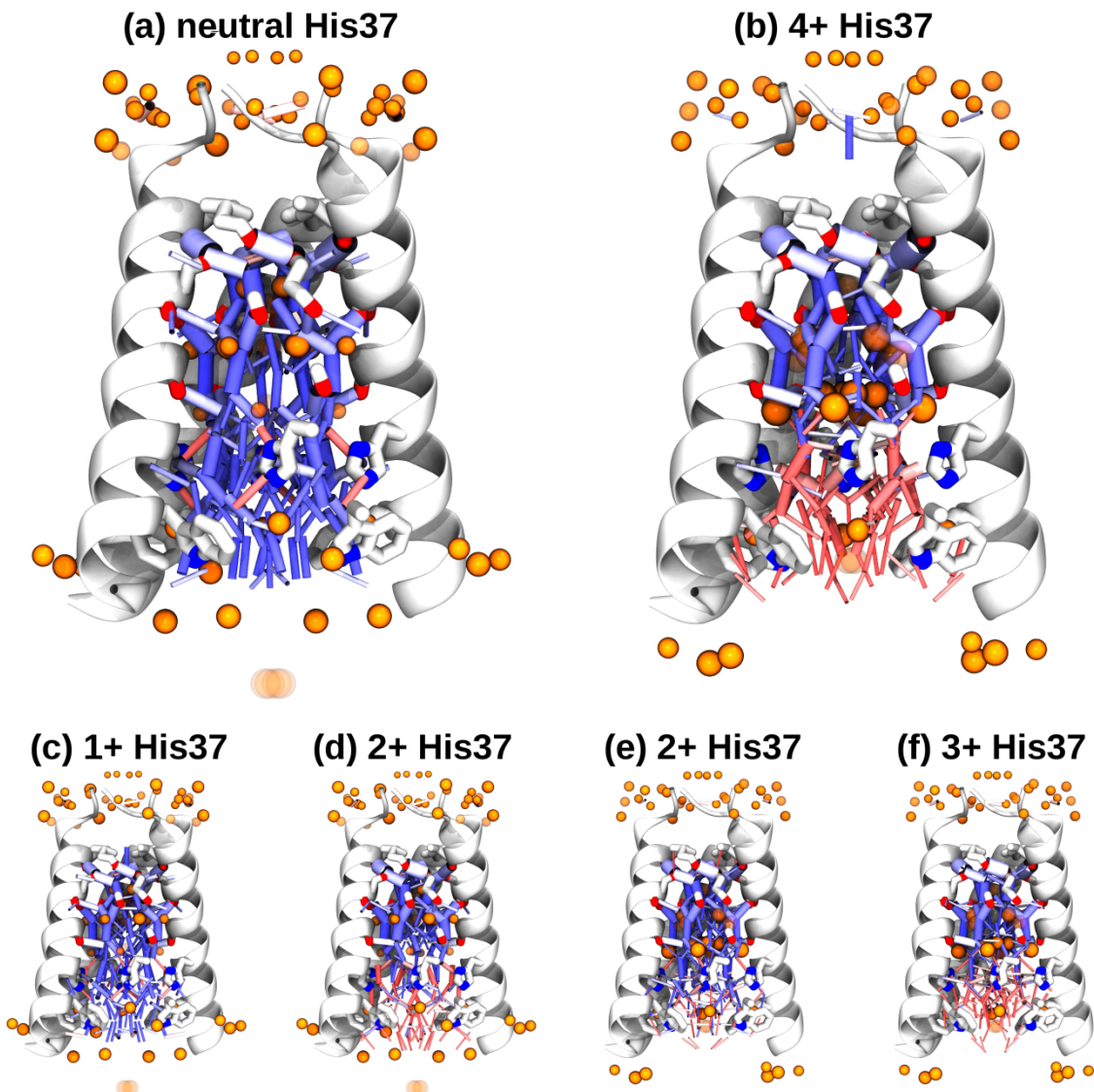


Figure S20. Water wires calculated from the molecular dynamics simulations at different charge states of the His37 tetrad for the D44N mutant. The oxygen atoms of the water molecules observed in the room temperature X-ray structures are shown as orange van der Waals spheres (orange color), with the diameter proportional to the crystallographic B-factors and transparency reflecting partial occupancy. Hydrogen bonds are represented as sticks, with a color scale denoting their orientation (see panels a-d), and thickness proportional to their population. **a** and **c-d**, Water wires for the 0, 1+ and 2+ charge states, respectively, for the production simulations starting from the cryogenic high pH crystal structure (PDB entry 4QK7). **b** and **d-e**, Water wires at the 4+, 2+ and 3+ charge states, respectively, for the production simulations starting from the cryogenic low pH crystal structure (PDB entry 4QKC).

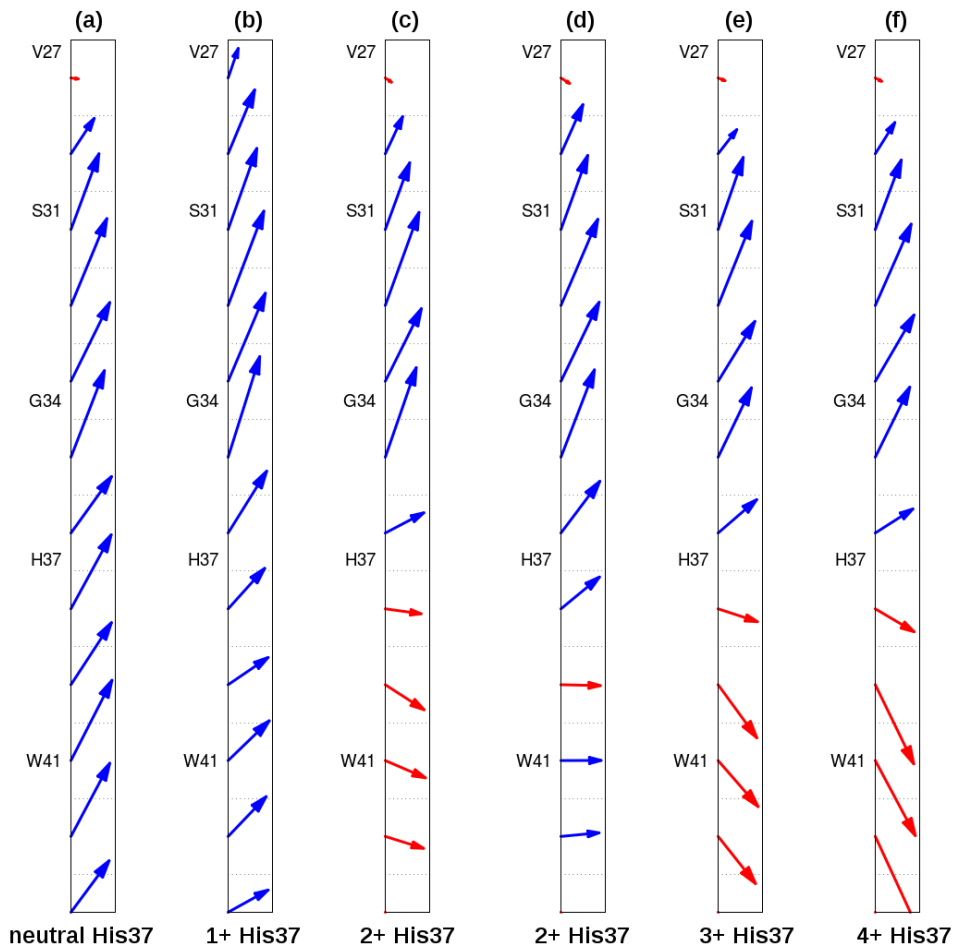


Figure S21. Average hydrogen bond vectors along the M2 pore at different charge states of the His37 tetrad for the D44N mutant. The vector direction reflects the net orientation with respect to the pore axis, with the H-bonds pointing to the exterior of the channel (outwards) colored in blue and the ones pointing to the viral interior (inwards) in red. The vector length is proportional to the magnitude of the net hydrogen bond (i.e. the longer, the larger the preference to be oriented in that direction). The hydrogen bonds are averaged over 2 Å bins along the pore axis (delimited by dashed black lines). **a-c**, Average hydrogen bond vectors at the 0, 1+, 2+ charge states, respectively, for the production simulations starting from the high pH cryogenic crystal structure (PDB entry 4QK7). **d-f**, Average hydrogen bond vectors at the 2+, 3+, 4+ charge states, respectively, for the production simulations starting from the low pH cryogenic crystal structure (PDB entry 4QKC).

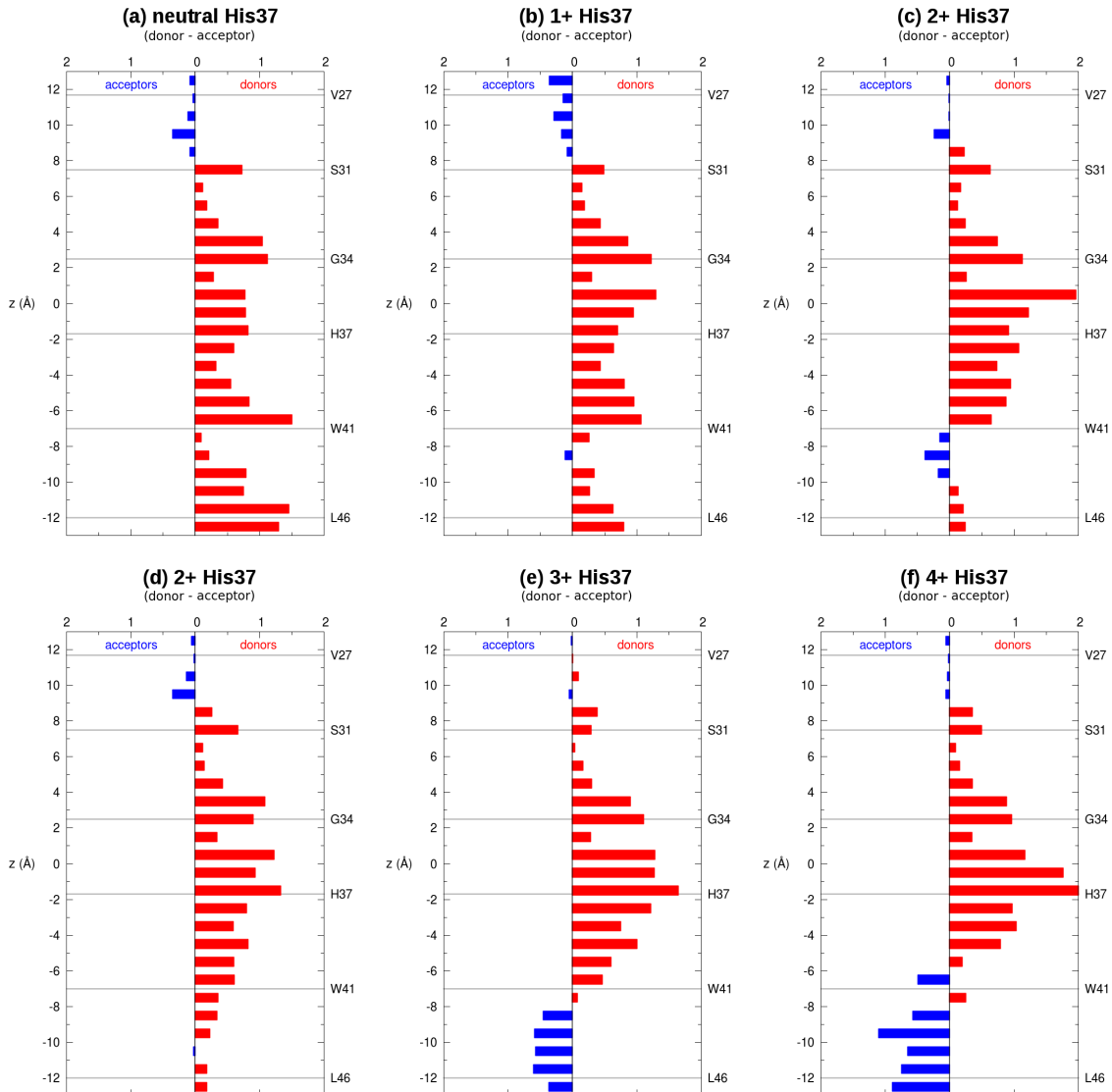


Figure S22. Difference between the number of water molecules acting as hydrogen bond donors and acceptors at different charge states of the His37 tetrad for the D44N mutant. The (*donor-acceptor*) difference along the M2 pore axis (z , in Å) is shown. Red bars represent a net number of donors at that pore position and blue bars a net number of acceptors. The position of the pore-lining M2 residues (C_α atom of Val27, Ser31, Gly34, His37, Trp41 and Leu46) is indicated by horizontal grey lines. **Top:** **a-c**, Difference (*donor-acceptor*) at the 0, 1+ and 2+ charge states, respectively, for the production simulations starting from the cryogenic high pH crystal structure (PDB entry 4QK7). **d-f**, Difference (*donor-acceptor*) at the 2+, 3+ and 4+ charge states, respectively, for the production simulations starting from the cryogenic low pH crystal structure (PDB entry 4QKC).

Table S5. Comparison of the C α RMSD and p values along the MD simulations of wild-type, S31N and D44N M2TM.

<i>4QKC-based simulations</i>			
RMSD (Å)	2+ His37	3+ His37	4+ His37
wild-type	0.77 ± 0.07	0.63 ± 0.06	0.76 ± 0.07
S31N	0.65 ± 0.07	0.67 ± 0.06	0.81 ± 0.07
D44N	0.79 ± 0.15	1.04 ± 0.18	0.70 ± 0.07
p	2+ His37	3+ His37	4+ His37
wild-type	0.60 ± 0.02	0.67 ± 0.02	0.63 ± 0.02
S31N	0.66 ± 0.02	0.68 ± 0.02	0.64 ± 0.02
D44N	0.60 ± 0.04	0.55 ± 0.04	0.62 ± 0.02

<i>4QK7-based simulations</i>			
RMSD (Å)	neutral His37	1+ His37	2+ His37
wild-type	0.75 ± 0.13	0.75 ± 0.07	1.09 ± 0.09
S31N	0.76 ± 0.06	0.72 ± 0.07	1.27 ± 0.08
D44N	0.56 ± 0.06	0.75 ± 0.10	0.65 ± 0.07
p	2+ His37	3+ His37	4+ His37
wild-type	0.60 ± 0.02	0.67 ± 0.02	0.63 ± 0.02
S31N	0.66 ± 0.02	0.68 ± 0.02	0.64 ± 0.02
D44N	0.60 ± 0.04	0.55 ± 0.04	0.62 ± 0.02

Experimental methods:

Synthesis and purification of M2(22-46)

The peptide construct used in this study is M2(22-46) from influenza A/Udorn/307/1972 . The peptide was synthesized on Rink Amide resin using a Quest 210 peptide synthesizer (Argonaut Technologies) at a temperature of 75°C for deprotection and coupling steps. Each residue was deprotected in a solution of 5% w/w piperazine and 0.1 M HOBr. For each coupling reaction, 5 molar equivalents of amino acid were pre-activated with 5 equivalents of HCTU and 10 equivalents of DIEA then this pre-activated mixture was added to the resin. After all of the amino acids were added to the resin, the reaction was cooled to 20°C and the N-terminus of the peptide was acylated by the addition of 20 equivalents of acetic anhydride and 40 equivalents of DIEA. The resin was washed with DCM and hexane then the peptide was cleaved from the resin in a mixture of 94% v/v TFA, 5% TES, and 1% H₂O. The resin was filtered out from the peptide-containing cleavage solution and washed with TFA, the excess TFA was blown off with a stream of nitrogen gas, then the peptide was precipitated into ether that had been chilled with dry ice. The mass of the resulting cleavage products was then confirmed by MS on a 3200 Q Trap LC/MS/MS (AB Sciex).

The peptide was purified using reverse-phase HPLC on a Varian ProStar purification system using a PROTO300 C4 10 µm column (Higgins Analytical Inc.). A gradient combining buffers A (99.9% water and 0.1% TFA) and B' (60% isopropanol, 30% acetonitrile, 10% water, 0.1% TFA) was used to separate and elute the peptide. A high degree of purity was necessary for the crystallization trials; analytical HPLC was used to confirm the degree of purity. The fractions of purified peptide were pooled and dissolved in ethanol. The concentration of peptide in the ethanol stock was determined by measuring the sample's absorbance at 280nm, then the stock solutions of peptide dissolved in ethanol were stored at -80°C.

Preparation of the lipidic cubic phase and crystallization

The lipidic cubic phase was prepared with some modifications to the protocol described by Caffrey and Cherezov¹. Peptide stock containing 4.0x10⁻⁷ moles of peptide in ethanol was added to 60mg of monoolein, mixed, then lyophilized overnight. The resulting peptide/monoolein mixture was warmed to 40°C in a water bath and transferred to a gas-tight Hamilton 250 µL syringe. 50 mM octylglucopyranoside (OG) in water was added into the syringe at a ratio of 20 µL for every 30 mg transferred sample, then the sample was then re-heated to 40°C and connected to a second gas-tight Hamilton syringe using a metal syringe coupler. The sample was pushed back and forth through the syringe coupler to mix; the appearance of the sample became transparent and homogenous after 1-2 minutes of transfer between the two syringes via the syringe coupler.

Crystallization conditions were screened in 96-well plastic plates (Molecular Dimensions) that were set up with a LCP crystallization robot (Anachem) using a protocol that combined 100 nL of monoolein/peptide sample with 1000 nL of screening solution. Square-shaped crystals belonging to space group I₄ formed after 2-4 weeks of incubation at 10°C. These conditions were optimized to grow 20-120 µm large crystals using the Hampton Additive screen. The crystals used for data collection at cryogenic conditions were grown in 96-well plates at 10°C then observed and harvested into liquid nitrogen in a 4°C cold room. The conditions that yielded the cryo high pH structure were: 0.18 M CaCl₂, 0.09 M Tris pH 8.0, 39.6% v/v PEG 400, 0.01 M β-nicotinamide adenine dinucleotide hydrate additive; the conditions that yielded the cryo low pH structure were: 0.18 M CaCl₂, 0.09 M MES pH 5.5, 39.6% v/v PEG 400, 5% v/v Jeffamine M-600 pH 7.0 additive in the presence of amantadine at a 4:1 ratio of Amt to tetramer, though density for the amantadine was not present in the crystal structure under these conditions and low pH crystals without amantadine yielded the same structure but at slightly lower resolution. Because of the high percentage of PEG 400 in the solution, no additional

cryoprotectant was added before the crystals were frozen and stored in liquid nitrogen. The crystals used for room temperature data were grown in 96-well plates at 20°C then were observed, transported to the beam line and harvested at ambient temperature. The conditions that yielded the room temperature high pH structure were: 0.18 M CaCl₂, 0.09 M Tris pH 8.0, 39.6% v/v PEG 400, 3% w/v xylitol additive; the conditions that yielded the room temperature low pH structure were: 0.18 M CaCl₂, 0.09 M MES pH 5.5, 39.6% v/v PEG 400, 0.01 M MnCl₂ · 4H₂O additive.

Data collection

All crystallographic data was collected at the Advanced Light Source on beam 8.3.1. The beam size was 100 μm for all data sets; the detector used was a 3 x 3 CCD array (ADSC Q315r). Data from the two cryo condition crystals that diffracted to 1.1 Å were collected at a temperature of < 100K with a 13.0 keV beam and a detector-to-sample distance of 125 mm. The high pH cryo condition crystal (PDB entry 4QK7) was exposed to the beam for 6 seconds per frame and the low pH cryo condition crystal (PDB entry 4QKC) was exposed for 4 seconds per frame; both crystals were oscillated 1 degree during data collection. The room temperature data was collected at 273 K using room temperature data collection techniques; with a 11.111 keV beam and an aluminum foil attenuator for both data sets. The crystals were looped at the beam line and a MiTeGenMicroRT plastic capillary containing 8 μL of precipitant solution mixed with 2 μL deionized water was placed on top of the goniometer base to hydrate the crystals during data collection. The crystals accumulated radiation damage faster under room temperature diffraction conditions, so larger crystals (50-120 μm) had to be diffracted to obtain complete data sets. The low pH room temperature condition crystal (PDB entry 4QKM) was exposed to the beam for 3 seconds per frame with a detector-to-sample distance of 125 mm; the high pH room temperature condition crystal (PDB entry 4QKL) was exposed to the beam for one second per frame with a detector-to-sample distance of 150 mm; both crystals were oscillated 1 degree during data collection. The data used to solve the room temperature structures was limited to the first 60 frames to minimize the effects of radiation damage on data quality.

Data processing, phasing and refinement

Data processing was done in iMosflm². Phasing was done by molecular replacement in the Phenix suite using Phaser MR³ with chain A from PDB entry 3C9J⁴ as a search model, then refinement was carried out in Phenix Refine⁵. Protein model manipulation and addition of water and ions were done in Coot⁶, and monoolein molecules were manually fit into Fo-Fc density using both Coot and PyMol⁷. Alternate conformers were predicted using the qFit web server⁸ and Ringer⁹, and were also manually added where positive Fo-Fc density indicated they were present. Anisotropic B-factors were used for both cryo conditions (PDB entries 4QK7 and 4QKC) and the low pH room temp condition (PDB entry 4QKM) but not the high pH room temp condition (PDB entry 4QKL).

Molecular dynamics simulation details

Classical molecular dynamics (MD) simulations of the hydrated protein crystal were performed to study the network of water molecules confined inside the M2 pore and its response to pH changes (i.e. the protonation state of His37). The initial configurations were built using the two cryo X-ray structures of the transmembrane region of the M2 bundle (M2TM, spanning residues 22-46) reported in this work (4QK7 and 4QKC, at high and low pH, respectively). In order to model the I_4 symmetry of the crystal, two staggered tetramers were included in the simulation box (see Supplementary Fig. S3), as well as the crystallographically resolved water molecules, monoolein molecules and calcium and chloride ions. Each of the four cryoprotectant molecules found inside the pore in the X-ray structures was replaced by two water molecules, occupying the same position of the two hydroxyl groups of ethylene glycol. The disordered lipidic phase was modeled as heptane, which provides a hydrophobic phase similar to monoolein with the advantage of faster equilibration, in the spirit of the highly mobile membrane mimetic used in another study¹⁰. A thin layer of water molecules was also added to fill out the unresolved hydrophilic region between the two tetramers, along with additional chloride ions to achieve neutrality. Simulations were performed starting from either the structure solved at low pH or the one at high pH (pH 5.5 and 8.0, respectively) for the five possible protonation states of the His37 tetrad (0, +1, +2, +3 and +4). The neutral histidine residues were set in the ϵ -tautomeric state and the histidine charge was increased by protonating one, two (non-adjacent), three or all four histidines, respectively, for each of the two tetramers. Each of the ten resulting systems consists of ~7,000 atoms.

The protein was modeled using the CHARMM force field^{11,12} with CMAP corrections¹³ and the water molecules were described using the TIP3P model¹⁴. The parameters by Roux and coworkers were used for the chloride¹⁵ and calcium¹⁶ ions. The heptane parameters were taken from the alkane force field^{17,18}. Mono-olein was parameterized using the CHARMM General Force Field (CGenFF, version 2b7)¹⁹ and the ParamChem server (version 0.9.6 beta)²⁰⁻²².

The simulations were performed in the NVT ensemble using the measured crystal lattice dimensions (29.310 Å x 29.310 Å x 67.310 Å for the low pH structure and 29.536 Å x 29.536 Å x 66.853 Å for the high pH) and applying periodic boundary conditions to mimic the crystal environment. Electrostatic interactions were calculated using the particle mesh Ewald (PME) method²³, with a real space spherical cutoff of 12 Å, an accuracy threshold of 10^{-6} and a fast Fourier transform (FFT) grid spacing of 0.8 Å (x and y dimensions) or 0.9 Å (z). Lennard-Jones interactions were cut off at 12 Å, with a switching function starting from 10 Å. The equations of motion were solved with the velocity Verlet integrator using a time step of 1.0 fs (equilibration) or 2.0 fs (productions runs). The lengths of the bonds involving hydrogen atoms were constrained with the SHAKE method²⁴. Each system was run at 310 K using a Langevin temperature coupling scheme²⁵, with a thermostat decay time of 1 ps.

The low pH and high pH structures (in the +4 and 0 protonation states, respectively) were pre-equilibrated for ~20 ns by applying harmonic restraining potentials on the position of the non-hydrogen atoms of the peptide backbone, the monoolein molecules and the crystallographic water and ions. The force constant (k) of the harmonic restraints was progressively reduced (from 20 to 2 kcal mol⁻¹ Å⁻² for the protein, from 10 to 4 kcal mol⁻¹ Å⁻² for the crystallographic water molecules and from 10 to 1 kcal mol⁻¹ Å⁻² for the other X-ray-derived moieties) in 0.5 ns steps. The resulting pre-equilibrated configurations of the 4+ and 0 states were used to build the initial models for the other protonation states. Upon change of the His 37 charge, each system was relaxed for ~10 ns using harmonic restraining potentials (with $k = 2$ kcal mol⁻¹ Å⁻² for the protein backbone, 4 kcal mol⁻¹ Å⁻² for the crystallographic water molecules and 1 kcal mol⁻¹ Å⁻² for monoolein and the X-ray derived ions). Then all harmonic restraints were released²⁶ and a production trajectory of ~300-450 ns was sampled for each system. All the MD simulations were performed with NAMD (version 2.9)²⁷. The stability of the

tetramer along the MD simulations was confirmed by examining the root mean square deviation (RMSD) of the C α atoms (see Supplementary Fig. S4).

Setup of the S31N mutant simulations

Classical MD simulations were performed for the S31N mutant of M2TM in order to assess the effect of the mutation in the number and directionality of the water wires inside the M2 pore. S31N is the most prevalent M2 mutation in circulating viruses and confers amantadine resistance while retaining conduction properties similar to wild-type M2. The initial configurations were built using equilibrated snapshots of the wild-type simulations and mutating *in silico* the residue at position 31 from serine to asparagine. The asparagine side chain was initialized in the same rotameric state as the NMR structure of the M2TM complex with thiophenyl-isoxazole-amantadine ($\chi_1 \approx -70^\circ$ and $\chi_2 \approx -30^\circ$; PDB code 2LY0). However, after a few nano seconds, it rotates and adopts a different rotameric state, with the amide group perpendicular to the pore axis ($\chi_1 \approx -80^\circ$ and $\chi_2 \approx -90^\circ$), and this conformation remains stable for the rest of the simulation.

The details of the classical MD simulations of the S31N mutant are identical to the wild-type. S31N M2TM was considered in each of the 5 possible protonation states of the His37 tetrad (0, 1+, 2+, 3+ and 4+). After an initial 20 ns equilibration with the protein backbone restrained, a production trajectory was sampled for 330 ns; only the last 250 ns were considered for the analysis. The stability of the mutant along the MD simulations was confirmed by examining the RMSD of the C α atoms (Fig. S11). Moreover, the protein conformation was maintained during the MD simulations, as can be seen by the stability of the principal component p (Fig. S12).

Setup of the D44N mutant simulations

Classical MD simulations were performed for the D44N mutant of M2TM in order to assess the effect of the loss of this C-terminal negative charge on the number and directionality of the water wires inside the M2 pore. The D44N mutation is present in the A/FPV/Rostock/34 influenza strain and results in enhanced proton conduction and loss of its asymmetry²⁸. Moreover, in contrast to the S31N mutant, the D44N mutant is still sensitive to amantadine, since this residue is located far from the drug binding site.

The initial configurations were built using equilibrated snapshots of the wild-type simulations and mutating *in silico* the residue at position 44 from aspartate to asparagine using the *Mutator* plugin of VMD³². Four chloride ions were also added for each tetramer in order to maintain neutrality. The details of the classical MD simulations of the D44N mutant are identical to the wild-type. D44N M2TM was considered in each of the 5 possible protonation states of the His37 tetrad (0, 1+, 2+, 3+ and 4+). After an initial 20 ns equilibration with the protein backbone restrained, a production trajectory was sampled for 330 ns; only the last 250 ns were considered for the analysis. The stability of the mutant along the MD simulations was confirmed by examining the RMSD of the C α atoms (Fig. S17). In addition, the partially dilated C-terminal protein conformation was maintained during the MD simulations (Fig. S18). The larger fluctuations of the protein backbone compared to the wild-type and the S31N mutant simulations (Table S5) are probably due to the modification of the protein-protein contacts of the crystal lattice, in which residue 44 is involved. Nevertheless, the structure of D44N M2TM is not significantly altered compared to the wild-type.

Analysis of the MD simulations

Principal component analysis. The protein backbone conformation of the crystallographic structures presented in this work lies between the C-terminal closed and dilated structures previously solved by X-ray or NMR (see main text). To characterize the backbone conformation of M2TM, we used the principal component p introduced in reference²⁸. In short, we computed difference vectors between each of the cryostructures in this work (either at low or at high pH, PDB entries 4QKC and 4QK7, respectively) and the X-ray structure solved at intermediate pH by Acharya and coworkers (PDB entry 3LBW²⁹), using the backbone coordinates of M2TM. Then we calculated the scalar product of this vector and the difference vector between the same intermediate pH structure²⁹ and the X-ray structure solved at low pH by Stouffer et al. (PDB entry 3C9J³⁰). The resulting quantity is the principal component p and it indicates the fraction of C-terminally closed *versus* dilated conformation of each of the two cryostructures. The obtained p values are 0.72 (low pH) and 0.73 (high pH), indicating that the C-terminus of the current M2TM structures is partially dilated. Moreover, the partially dilated protein conformation is maintained during the MD simulations, as can be shown by the stability of p as a function of simulation time in Supplementary Fig. S5.

Water densities. Water densities were obtained from the MD simulations using the Volmap plugin³¹ in VMD (version 1.9)³². Each water atom was treated as a normalized isotropic Gaussian density of width equal to 0.532 Å (oxygen) or 0.42 Å (hydrogen), that is their van der Waals radius scaled by 0.35. This radius scaling factor was chosen empirically by applying the Volmap plugin on the recently solved 0.88 Å resolution crystal structure of aquaporin³³; the calculated density reproduces the experimental density when scaling the atomic radii by 0.35. Besides, this is in line with the electron density of water in simulations being 0.34 e Å³ for TIP3P waters³⁴. The density was weighted by the atomic number ($z = 8$ or 1, respectively) and summed over all the pore waters using a three dimensional grid with a 0.25 Å bin resolution. The time average was taken over the last ~250 ns of the MD trajectories. Four-fold rotational symmetry was enforced by recalculating the water density after each of the four 90 degree rotations along the pore axis of the homotetramer and averaging the four resulting density maps. The obtained MD water densities are shown in Fig. 3a and Supplementary Fig. S2.

Populations of hydrogen bonds in the M2 pore. We calculated the populations of hydrogen-bonded water molecules using the following clustering protocol. We defined a hydrogen-bond vector between a donor and an acceptor when the two oxygen atoms are at a distance less than 3.5 Å and the donor-hydrogen-acceptor angle is between 150°-180°. Four-fold rotational symmetry was enforced by recalculating the hydrogen-bond vectors after each of the four 90 degree rotations along the pore axis of the homotetramer. We calculated the clusters of these vectors using g_cluster (version 4.5.5)³⁵ over ~250 ns-long MD trajectories (i.e. the first 100 ns were considered as equilibration and discarded). We used a cutoff equal to 1.5 Å to define hydrogen bond vectors as belonging to the same cluster. To obtain the occupancy of a hydrogen bond represented by the centroid of one cluster, we divided the population of the cluster by the total number of MD frames and by 4 (to normalize upon symmetrization), such that the occupancy of a given hydrogen bond is at most 1. Fig. 4 and Supplementary Fig. S7 are produced by drawing cylinders corresponding to each cluster, with the thickness determined by the corresponding occupancy and the color indicating the orientation (blue for hydrogen bonds oriented towards the exterior of the channel and red if oriented towards the viral interior, see Supplementary Fig. S7). These figures were made with the VMD program (version 1.9)³².

Density and orientation of hydrogen bonds. The density (in Å⁻³) and orientation (in Å⁻²) of hydrogen bond vectors (Supplementary Fig. S6) were calculated over the last ~250 ns of MD trajectory as follows:

1. The frames of the MD simulation are aligned onto the crystal cryostructure (using the backbone

atoms of residues 25-46 as reference) to remove diffusive motions of M2TM.

2. The oxygen atoms of all the water molecules forming hydrogen bonds with other water molecules or His37 in the M2 pore are selected and their two cylindrical coordinates (z and r) are computed. z is the Cartesian coordinate that indicates the displacement along the pore axis (with origin on the center of mass of M2TM 25-46), whereas r is the radial distance from the pore axis.
3. The corresponding hydrogen bond vectors $hb(r,z)$ are calculated as the difference between the cylindrical coordinates of the acceptor and the donor.
4. The density of hydrogen bond vectors $n_{hb}(r,z)$ (shown in black in Supplementary Fig. S6) is computed as a two-dimensional histogram of the number of hydrogen bond vectors, with a grid of 0.2 Å spacing. Thereby, we are performing a cylindrical average over r , that is over the four M2 monomers. The orientation of hydrogen bond vectors $n_{hb}(r,z)$ (shown in red and blue in Supplementary Fig. S6) is computed in a similar way, but considering the direction of the vector, so that a hydrogen bond has a positive contribution if oriented outwards or negative if oriented inwards.
5. The two-dimensional histograms are normalized with weighting factor ($\frac{1}{2}\pi r$) to allow a visual comparison of the density near the pore axis with respect to the density at large values of r , where atoms are more numerous for geometrical reasons.
6. The normalized density is plotted using a color scale ranging from white (0 Å⁻³) to full black (0.05 Å⁻³), whereas for the normalized orientation color scale spans from full red (-0.025 Å⁻²) to white (0 Å⁻²) and then to full blue (+0.025 Å⁻²).

Average number of hydrogen bonds. We calculated the number of hydrogen bonds inside the M2 pore, averaged over the last ~250 ns of the MD trajectory. Only water-water and water-His37 hydrogen bonds were considered and they were classified as extraviral or intraviral depending on whether the donor and acceptor water oxygen atoms were above or below the His37 tetrad (i.e. extraviral if z (donor O) and z (acceptor O) > z (center of mass of the His37 tetrad) and intraviral if otherwise). Hydrogen bonds are oriented outwards if z (donor O) < z (acceptor O), whereas they are oriented inwards if z (donor O) > z (acceptor O). This analysis, shown in Supplementary Table S2, is intended to provide a more quantitative picture of the hydrogen bond population displayed in Fig. 4 and Supplementary Fig. S7.

Average hydrogen bond vectors along the M2 pore axis. We calculated the average hydrogen bond vectors along the pore axis (z) using the hydrogen bond vectors expressed in spherical coordinates $hb(r,z)$, calculated as explained above. These individual vectors were averaged over the last ~250 ns of the MD trajectory and over 2 Å bins along the pore axis; $hb(r,z)$ is considered to belong to a certain z slab if the floor of z (donor O) = z (slab). The resulting average vectors are shown in Supplementary Fig. S8. Their direction reflects the orientation with respect to the pore axis (i.e. upwards indicates a net number of hydrogen bonds directed towards the exterior of the channel and downwards towards the viral interior), whereas their length is proportional to the magnitude of the net hydrogen bond vector (i.e. the longer, the larger the preference to be oriented in that direction). These average hydrogen bond vectors (Supplementary Fig. S8) present a one-dimensional, more simplified picture of the two-dimensional histograms in Supplementary Fig. S6.

Average number of donors and acceptors along the pore. We calculated the difference between the number of water molecules acting as hydrogen bond donors and acceptors along the pore axis z . Compared to the previous analyses, in which we calculated only the water-water and water-His37 hydrogen bond vectors, here we calculated the number of water molecules donating or accepting hydrogen bonds to or from other water molecules and the protein (i.e. carbonyl oxygen atoms, Ser31 hydroxyl group or Asn31 amide group and His37 imidazole). The (*donor*–*acceptor*) difference is

averaged over the last ~250 ns of the MD trajectory and over 2 Å bins along the pore axis; a water molecule is considered to belong to a certain z slab if the floor of z (oxygen atom) = z (slab). The average differences along z are shown as bar graphs in Supplementary Fig. S9. A red bar indicates a net number of water molecules acting as H-bond donors, whereas a blue bar represents a net number of water molecules acting as H-bond acceptors.

Control simulations

Besides the production MD described above, we also performed control simulations with all X-ray derived water molecules restrained at their crystallographic positions. Two types of control simulations were run:

1. “restrained” simulations, in which the cryogenic X-ray structures at high and low pH (PDB entries 4QK7 and 4QKC, respectively) were simulated while applying a restraining harmonic potential on the oxygen atoms of the crystallographic water molecules;
2. “swapped” simulations, where the crystallographic water molecules in the cryogenic high pH structure (PDB entry 4QK7) were replaced by those of the low pH structure (PDB entry 4QKC), and vice versa; the resulting chimeric systems were simulated using a harmonic restraining potential on the grafted water molecules.

The harmonic force constant (k) used in both types of control simulations is 4 kcal mol⁻¹ Å⁻² (that is, each water oxygen atom can fluctuate ±0.5 Å around its experimental position), except for water molecules 35 and 47 in the high pH structure, for which k = 1 kcal mol⁻¹ Å⁻² (±1.1 Å oscillations). Water 35 of one M2TM monomer is only 1.26 Å apart of water 47 of another monomer, and either of them can form a H-bond with water 36, indicating that the water sites 35 and 47 are alternatively occupied. The rest of the simulation details are the same as for the production MD (see above). Control simulations were run for all five possible protonation states of the His37 tetrad (0, 1+, 2+, 3+ and 4+) and a trajectory of ~120 ns was sampled for each system. For each control simulation, the first ~20 ns were discarded as equilibration and the population of hydrogen bonds was calculated on the last ~100 ns, following the same clustering protocol as for the production simulations (see above). The obtained water wires are shown in Supplementary Fig. S10.

The distribution of H-bond donors and acceptors in the restrained simulations (Supplementary Fig. S10, panels a-d) is nearly identical to the production MD (Fig. 4 and Supplementary Fig. S7). Therefore, the computational water model (TIP3P¹⁴) is able to accurately predict the hydrogens’ positions, despite the slight differences between the experimental and calculated water densities. On the other hand, the orientation of hydrogen bonds in the restrained simulations (Supplementary Fig. S10, panels a-d) is almost indistinguishable from the swapped simulations (Supplementary Fig. S10, panels e-h). This indicates that the hydrogen bond orientation does not depend on the precise position of the water molecules, and it is determined only by the charge state of the His37 tetrad.

References

- 1 Caffrey, M. & Cherezov, V. Crystallizing membrane proteins using lipidic mesophases. *Nat. Protoc.* **4**, 706-731, doi:10.1038/nprot.2009.31 (2009).
- 2 Battye, T. G. G., Kontogiannis, L., Johnson, O., Powell, H. R. & Leslie, A. G. W. iMOSFLM: a new graphical interface for diffraction-image processing with MOSFLM. *Acta Crystallogr. Sect. D-Biol. Crystallogr.* **67**, 271-281, doi:10.1107/s0907444910048675 (2011).
- 3 McCoy, A. J. *et al.* Phaser crystallographic software. *J. Appl. Crystallogr.* **40**, 658-674, doi:10.1107/s0021889807021206 (2007).
- 4 Stouffer, A. L. *et al.* Structural basis for the function and inhibition of an influenza virus proton channel. *Nature* **451**, 596-U513, doi:10.1038/nature06528 (2008).
- 5 Adams, P. D. *et al.* PHENIX: a comprehensive Python-based system for macromolecular structure solution. *Acta Crystallogr. Sect. D-Biol. Crystallogr.* **66**, 213-221, doi:10.1107/s0907444909052925 (2010).
- 6 Emsley, P., Lohkamp, B., Scott, W. G. & Cowtan, K. Features and development of Coot. *Acta Crystallogr. Sect. D-Biol. Crystallogr.* **66**, 486-501, doi:10.1107/s0907444910007493 (2010).
- 7 Schrodinger, LLC. *The PyMOL Molecular Graphics System, Version 1.3r1* (2010).
- 8 van den Bedem, H., Dhanik, A., Latombe, J. C. & Deacon, A. M. Modeling discrete heterogeneity in X-ray diffraction data by fitting multi-conformers. *Acta Crystallogr. Sect. D-Biol. Crystallogr.* **65**, 1107-1117, doi:10.1107/s0907444909030613 (2009).
- 9 Lang, P. T. *et al.* Automated electron-density sampling reveals widespread conformational polymorphism in proteins. *Protein Sci.* **19**, 1420-1431, doi:10.1002/pro.423 (2010).
- 10 Ohkubo, Y. Z., Pogorelov, T. V., Arcario, M. J., Christensen, G. A. & Tajkhorshid, E. Accelerating membrane insertion of peripheral proteins with a novel membrane mimetic model. *Biophys. J.* **102**, 2130-2139 (2012).
- 11 MacKerell, Jr., A. D., Bashford, D., Bellot, M., Dunbrack, R. L. Jr, Evanseck, J. D., Field, M. J., Fischer, S., Gao, J., Guo, H. & Ha S. All-atom empirical potential for molecular modeling and dynamics studies of proteins. *J. Phys. Chem. B* **102**, 3586–3616 (1998).
- 12 MacKerell, Jr., A. D., Feig, M. and Brooks, III, C. L. Improved treatment of the protein backbone in empirical force fields. *J. Am. Chem. Soc.* **126**, 698-699 (2004).
- 13 Best, R. B., Zhu, X., Shim, J., Lopes, P., Mittal, J., Feig, M. and MacKerell, Jr., A. D.. Optimization of the additive CHARMM all-atom protein force field targeting improved sampling of the backbone phi, psi and sidechain chi1 and chi2 dihedral angle. *J. Chem. Theory Comput.* **8**, 3257-327 (2012).

- 14 Jorgensen, W. L., Chandrasekhar, J., Madura, J. D., Impey, R. W. & Klein, M. L. Comparison of simple potential functions for simulating liquid water. *J. Chem. Phys.* **79**, 926–935 (1983).
- 15 Beglov, D. & Roux, B. Finite Representation of an infinite bulk System: solvent boundary potential for computer simulations. *J. Chem. Phys.* **100**, 9050-9063 (1994).
- 16 Marchand, S. & Roux, B. Molecular dynamics study of calbindin D9k in the apo and singly and doubly calcium-loaded states. *Proteins*, **33**, 265–284 (1998).
- 17 Klauda, J. B., Venable, R. M., Freites, J. A., O'Connor, J. W., Tobias, D. J., Mondragón-Ramírez, C., Vorobyov, I., MacKerell, Jr., A. D. & Pastor, R. W. Update of the CHARMM all-atom additive force field for lipids: validation on six lipid types. *J. Phys. Chem. B* **114**, 7830-7843 (2010).
- 18 Lee, S., Tran, A., Allsopp, M., Lim, J. B., Hénin, J. & Klauda, J. B. CHARMM36 united-atom chain model for lipids and surfactants. *J. Phys. Chem. B* **118**, 547–556 (2014).
- 19 Vanommeslaeghe, K., Hatcher, E., Acharya, C., Kundu, S., Zhong, S., Shim, J., Darian, E., Guvench, O., Lopes, P., Vorobyov, I. & MacKerell, Jr., A. D. CHARMM general force field: a force field for drug-like molecules compatible with the CHARMM all-atom additive biological force fields. *J. Comput. Chem.* **31**, 671–90 (2009).
- 20 Vanommeslaeghe, K. & MacKerell, Jr., A. D. Automation of the CHARMM General Force Field (CGenFF) I: bond perception and atom typing, *J. Chem. Inf. Model.* **52**, 3144-3154 (2012).
- 21 Vanommeslaeghe, K., Raman, E. P. & MacKerell, Jr., A. D. Automation of the CHARMM General Force Field (CGenFF) II: Assignment of bonded parameters and partial atomic charges, *J. Chem. Inf. Model.* **52**, 3155-3168 (2012).
- 22 www.paramchem.org
- 23 Essman, U., Perera, L., Berkowitz, M. L., Darden, T., Lee, H. & Pedersen, L. G. A smooth particle mesh Ewald method. *J. Chem. Phys.* **103**, 8577–8592 (1995).
- 24 Ryckaert, J.-P., Ciccotti, G. & Berendsen, H. J. C. Numerical integration of the cartesian equations of motion of a system with constraints: molecular dynamics of N-alkanes. *J. Comput. Phys.* **23**, 327– 341 (1977).
- 25 Adelman, S. A. & Doll, J. D. Generalized Langevin equation approach for atom/solid-surface scattering: General formulation for classical scattering off harmonic solids. *J. Chem. Phys.* **64**, 2375-2388 (1976).
- 26 Previous simulations of M2-TM in a membrane (Wei, C. & Pohorille, A. Activation and proton transport mechanism in influenza A M2 channel. *Biophys. J.* **105**, 2036-2045 (2013) and Gkeka, P., Eleftheratos, S., Kolocouris, A & Couronia, Z. Free energy calculations reveal the origin of binding preference for aminoadamantane blockers of influenza. *J. Chem. Theory Comput.* **9**, 1272-1281 (2013)) have shown that anions, such as chloride, can access the interior of the M2 pore. In our crystal environment simulations, entrance of Cl⁻ is overestimated due to

- the limited volume of water between the two staggered tetramers. Therefore, we have used a wall-like restraining potential to penalize the presence of chloride ions inside the pore and thus sample the pore hydration without anion-induced perturbations.
- 27 Phillips, J. C., Braun, R., Wang, W., Gumbart, J., Tajkhorshid, E., Villa, E., Chipot, C., Skeel, R. D., Kalé, L. & Schulten, K. Scalable molecular dynamics with NAMD. *J. Comput. Chem.* **26**, 1781-1802 (2005).
- 28 Ma, C., Fiorin, G., Carnevale, V., Wang, J., Lamb, R. A., Klein, M. L., Wu, Y., Pinto, L. H. & DeGrado, W. F. Asp44 stabilizes the Trp41 gate of the M2 proton channel of influenza A virus. *Structure* **21**, 2033-2041 (2013).
- 29 Acharya, R., Carnevale, V., Fiorin, G., Levine, B.G., Polishchuk, A.L., Balannik, V., Samish, I., Lamb, R.A., Pinto, L.H., DeGrado, W.F. & Klein, M.L. Structure and mechanism of proton transport through the transmembrane tetrameric M2 protein bundle of the influenza A virus. *Proc. Natl. Acad. Sci. USA* **107**, 15075-15080 (2010).
- 30 Stouffer, A.L., Acharya, R., Salom, D., Levine, A.S., Costanzo, L.D., Soto, C.S., Tereshko, V., Nanda, V., Stayrook, S. & DeGrado, W.F. Structural basis for the function and inhibition of an influenza virus proton channel. *Nature* **451**, 596-600 (2008).
- 31 Cohen, J., Arkhipov, A., Braun, R. & Schulten, K. Imaging the migration pathways for O₂, CO, NO, and Xe inside myoglobin." *Biophysical Journal* **91**, 1844-1857 (2006).
- 32 Humphrey, W., Dalke, A. & Schulten, K. VMD-Visual Molecular Dynamics. *J. Mol. Graphics* **14**, 33-38 (1996).
- 33 Kosinska Eriksson, U., Fischer, G., Friemann, R., Enkavi, G., Tajkhorshid, E. & Neutze, R. Subangstrom resolution X-ray structure details aquaporin-water interactions. *Science*. **340**, 1346-1349 (2013).
- 34 Klauda, J. B., Kucherka, N., Brooks, B. R., Pastor, R. W. & Nagle, J. F. Simulation-based methods for interpreting X-ray data from lipid bilayers. *Biophys. J.* **90**, 2796-2807 (2006).
- 35 Daura, X., Gademann, K., Jaun, B., Seebach, D., van Gunsteren, W. F. & Mark, A. E. Peptide folding: when simulation meets experiment. *Angew. Chem. Int. Ed.* **38**, 236-240 (1999).